Two Classes of Unconventional Photonic Crystals

by

Y. D. Chong

B.S. Physics
Stanford University, 2003

SUBMITTED TO THE DEPARTMENT OF PHYSICS IN PARTIAL
FULFILLMENT OF THE REQUIREMENTS FOR THE DEGREE OF

DOCTOR OF PHILOSOPHY
AT THE
MASSACHUSETTS INSTITUTE OF TECHNOLOGY

AUGUST 2008

Signature of Author: ————————————————————
Department of Physics
August 2008

Certified by: ————————————————————
Marin Soljačić
Assistant Professor of Physics
Thesis Supervisor

Accepted by: ————————————————————
Professor Thomas J. Greytak
Associate Department Head for Education

Abstract

This thesis concerns two classes of photonic crystal that differ from the usual solid-state dielectric photonic crystals studied in optical physics.

The first class of unconventional photonic crystal consists of atoms bound in an optical lattice. This is a "resonant photonic crystal", in which an underlying optical resonance modifies the usual band physics. I present a three-dimensional quantum mechanical model of exciton polaritons which describes this system. Amongst other things, the model explains the reason for the resonant enhancement of the photonic bandgap, which turns out to be related to the Purcell effect. An extension of this band theoretical approach is then used to study dark-state polaritons in Λ-type atomic media.

The second class of unconventional photonic crystal consists of two dimensional photonic crystals that break time-reversal symmetry due to a magneto-optic effect. The band theory for such systems involves topological quantities known as "Chern numbers", which give rise to the phenomenon of disorder-immune one-way edge modes. I describe a system in which time-reversal symmetry is broken strongly enough for experimental observation of the one-way edge modes. In addition to numerical studies of this photonic crystal, I develop an analytical effective theory, based on the symmetry of the lattice, that accurately describes its bandstructure.

For my parents.

Contents

List of Figures

Introduction

Since the pioneering work of John[1], it has been recognized that systems with optical properties that vary at optical length-scales—now known as photonic crystals—possess remarkable properties that can be used to manipulate the flow of light. The conventional theory of photonic crystals proceeds by applying Maxwell's equations for the electromagnetic field to a "meta-material" with an index of refraction that varies periodically in space. It is then shown that these equations reduce to a Hermitian eigenproblem, analogous to the Schrödinger equation with a periodic Hamiltonian[2]. Due to the partial breaking of continuous translational symmetry induced by the periodic variation in the refractive index, the normal modes of the electromagnetic field are separated into discrete bands, similar to electronic bands in crystalline solids[3]. At the length-scale of the lattice spacing, the optical dispersion can deviate significantly from its character in bulk media, leading to diverse phenomena such as photonic stop-bands (complete bandgaps): frequencies around which no modes exist at any wave-vector[4].

In this thesis, I will study two types of photonic crystal that deviate from

the conventional mold in interesting and quite different ways. The first consists of cold atoms bound in an optical lattice[5], within the "Mott insulator" regime where atomic hopping between lattice sites is negligible[6]. Such systems have been intensively studied within the atomic physics community, though not usually from the point of view, originally explored by Deutsch, Spreeuw, Rolston, and Phillips[7], which I will adopt: that they are a type of "resonant photonic crystal" in which the lattice spacing falls near the wavelength of an underlying resonance—in this case, the Rabi frequency of the atoms. In such systems, the photonic bandgap, which is determined by the lattice spacing, can be enhanced by matching the bandgap frequency to the resonance frequency. (Resonant photonic crystals have also been realized in other contexts, such as meta-materials made of polaritonic media[8] or periodic arrays of quantum dots[9–11].) In Chapter 1, I will briefly review previous analyses of the cold-atom system, which treat the electromagnetic field classically and the atoms as classical point dipoles[7,12], and then present a simple quantum mechanical model based on two-level atoms and a quantized electromagnetic field. In this model, the elementary excitations are polaritons: coherent quantum superpositions of atomic excitations and photons. Like the electromagnetic modes in conventional photonic crystals, the polaritons are divided into bands. The model reproduces several key features of the classical models; in particular, the interaction between the lattice spacing and the atomic resonance causes an enhancement of the polaritonic bandgap, and we shall see how this process can be viewed as a generalization of Rabi splitting

in a microcavity[13]. In Chapter 2, I will examine the polaritons arising from Λ-type atoms, in which each atom possesses an additional metastable state. Unlike two-level atoms, the optical properties of Λ-type atoms can be tuned by the application of "control beams" resonant with the transition to the metastable state[14]. As Fleischhauer and Lukin have shown, this leads to the existence of a "dark-state polariton" whose dispersion properties are determined by the control beams[15]. I will present a derivation of the polaritonic bandstructure in such systems.

The second type of photonic crystal that I will discuss is, like the conventional photonic crystal, a classical solid-state device—but one that breaks time-reversal symmetry. In ordinary dielectric media, time-reversal symmetry is never violated: if we solve Maxwell's equations to obtain the classical field amplitudes for a given system, the complex conjugate of the solution is an exact solution for the time-reversed system[2]. Time-reversal symmetry can be broken by introducing magneto-optical materials, such as iron garnets; such materials are employed in Faraday rotators, commonly-used devices that reduce the backscattering of guided light by filtering out the reversed optical modes. For several years, various authors have investigated using magneto-optical materials in photonic crystals, for purposes such as enhancing the Faraday rotation effect. However, it was Haldane and Raghu who first pointed out what I believe to be the most remarkable and unique consequence of time-reversal symmetry-breaking in photonic crystals[16,17]: by drawing an analogy between the quantum Hall system (a two-dimensional electronic fluid

in the presence of a strong magnetic field[18]) and two-dimensional magneto-optical photonic crystals, these authors predicted that properly-engineered crystals can support "one-way edge modes" that lie within a photonic stop-band and lack time-reversed companion modes. Like "chiral edge states" in the quantum Hall effect, the existence of these edge modes is tied to the topological properties of the time-reversal symmetry-broken bandstructure, which cannot be altered affected by any perturbative distortion of the lattice including the existence of (sufficiently weak) defects. In Chapter 3, I will describe a gyromagnetic photonic crystal that provides an experimentally-feasible system containing one-way edge modes, and present numerical simulations that demonstrate the robustness of these modes. In Chapter 4, I investigate the bandstructure of this crystal in greater detail, by developing an effective Hamiltonian that accurately describes the bands in the regime where the symmetries of the crystal are weakly broken. Among other results, the topological band properties, which are tied to the existence of one-way edge modes, can be analytically determined within this theory.

Acknowledgements

Some of the work presented in this thesis has been previously published as separate papers; I have provided a journal reference to the corresponding paper at the beginning of each chapter. These papers were all co-written with Prof. Marin Soljačić, my research advisor; as well as Prof. David Pritchard (Chapter 1), Dr. Zheng Wang and Prof. John Joannopolous (Chapter 3), and Prof. Xiao-Gang Wen (Chapter 4). I would like to thank them all for wonderful and fruitful collaborations, and Marin in particular for his invaluable guidance.

I have also benefited from discussions with Prof. Steven Johnson, Maissam Barkeshli, Peter Bermel, Jorge Bravo-Abad, Ardavan Farjadpour, Alexander McCauley, and Alejandro Rodriguez. To them, and to the rest of the theoretical condensed matter physics community at MIT, I extend my sincere gratitude.

Finally, I would like to thank Jiamin Chin; all my friends in the Singaporean community at MIT; and my parents, S. K. Chong and L. S. Goh, to whom this thesis is dedicated.

Chapter 1

Polaritons in a Point-dipole Crystal

1.1 Exciton polaritons in optical lattices

The optical lattice is one of the most remarkable technologies to arise from
the field of atomic and optical physics during the last few decades[5]. When
interfering laser beams are applied to a system of cold atoms, the AC Stark
interaction between the atoms and the laser field induces a periodic structure
within the atomic system. At low laser intensities, the atoms exist in a su-
perfluid phase in which the number of atoms at each lattice site is ill-defined;
as the intensity increases, the superfluid undergoes a series of phase transi-
tions into Mott-insulator phases with an integral number $(n = 1, 2, 3, \cdots)$ of

---

atoms per site[6]. Such a transition was observed experimentally in 2002 by Greiner *et. al.*[19]

Early in the development of optical lattices, Deutsch, Spreeuw, Rolston, and Phillips[7] pointed out that an optical lattice can be thought of as a kind of photonic crystal, since the lattice spacing is one-half the laser wavelength and thus (obviously) comparable to optical wavelengths. This led to the following puzzle: in a photonic crystal, there is usually a photonic band gap at wavevectors coinciding with the Brillouin zone boundary, due to Bragg scattering. In an optical lattice, the applied laser beams fall exactly on the Brillouin zone boundary, which seems to imply that the optical lattice prohibits the propagation of the same light that supports its existence! As we shall see, the situation can be resolved by noting that the optical lattice is a special kind of photonic crystal—a "resonant photonic crystal"—in which the underlying medium possesses an optically-active resonance. Typically, resonant photonic crystals contain an additional band that meets the light line at the Brillouin zone boundary. In the case of the optical lattice, the resonance is simply the atomic transition through which the atoms interact with the applied laser fields, and the laser fields are allowed to fill the lattice because they fall exactly on this additional band. When the lattice spacing is tuned to the resonance frequency, this additional band has vanishingly low group velocity and occupies the middle of the photonic band gap.

Many authors have studied how optically-active resonances affect the electromagnetic modes in a lattice, beginning long before the invention of optical

lattices. Originally, interest in the subject arose within the field of solid-state physics. In 1958, Hopfield[20] wrote a seminal paper that showed how Frenkel excitons—the elementary electronic excitations in a tight-binding insulator— are modified by the interaction between the atoms and the electromagnetic field. Hopfield pointed out that when one considers the crystal and the elec- tromagnetic field as a unified quantum system, the elementary excitations are no longer simply Frenkel excitons and photons, but coherent mixtures of the two, which he called exciton polaritons. The polaritons' dispersion relation has a non-trivial bandstructure, with a gap at the optical resonance of the atoms. In subsequent sections, I will use the Hopfield theory as the basis for modelling optical lattices.

The polariton concept survives into the classical limit, and many authors have studied the problem in this regime, most notably Deutsche and Mead[21], and Mahan and Obermair[22]. Here, instead of modelling each atom as (say) a two-level quantum system, one treats it as a localized classical dipole. The excitation frequency of the Frenkel excitons is replaced by the natural oscillation frequency of the classical dipoles, and the polaritons are normal modes of the classical electromagnetic field, which can be obtained by solving Maxwell's equations.

Such an approach was taken by Deutsch *et. al.*[7], in 1995, to investigate the nature of the electromagnetic modes in an optical lattice. As mentioned earlier, it was they who pointed out that an optical lattice is a type of pho- tonic crystal. Previously, authors studying the point-dipole crystal implicitly

assumed that the lattice spacing was much smaller than the wavelength of the polaritons. For solid-state systems, this is a rather good assumption: the atomic spacing is around 10^{-10} m, whereas polaritonic effects occur at wavelengths corresponding to optical resonances, typically around 10^{-6} m. (One could, in principle, study X-ray resonances, but this introduces additional effects, such as Compton scattering, that lie outside the scope of the point-dipole model.) In optical lattices, as we have discussed, the two length scales are in fact comparable, and Bragg scattering plays an important role.

Deutsch *et. al.* studied a simple model of a 1D optical lattice consisting of an infinite periodic stack of polarizable planes. In this system, Maxwell's equations can solved using a transfer-matrix method, and they showed that the electromagnetic modes are gapped at a frequency near the dipole resonance frequency and a wavelength of one-half the lattice spacing (i.e. the edge of the first Brillouin zone, $k = \pi/a$). This band gap arises from a combination of two effects: the presence of an optical resonance within the planes (like the point-dipole crystal models discussed earlier), and Bragg scattering (like an ordinary photonic crystal). They found that the center of the band-gap contains an additional branch of longitudinal electromagnetic modes with very low group velocity. These modes allow for the existence of the laser fields that support the optical lattice.

A three-dimensional version of this calculation was performed by van Coevorden *et. al.*[12] for the FCC lattice, using a higher-dimensional numerical generalization of the transfer-matrix method. Just like the 1D case, there is

a band gap at the resonance frequency and a low-velocity branch of longitudinal modes within that gap. Similar phenomena have been encountered in solid-state resonant photonic crystals, such as photonic crystals made from polaritonic materials[8] and multiple-quantum-well arrays[9–11].

In this chapter, I will develop a simple 3D quantum mechanical model of the optical lattice, starting with the Hopfield theory from which the exciton polariton concept was originally born[20]. As we shall see, the "resonant photonic crystal" effects discovered by Deutsch *et. al.* survive into the quantum mechanical regime. With quite resonable approximations, the properties of the quantum mechanical polaritons can be obtained analytically. Many of the features found in the classical system appear naturally, and with somewhat simpler interpretations. For instance, the enhancement of the photonic bandgap in a tuned lattice is shown to be analogous to the well-known Purcell effect (the enhancement of Rabi splitting in a microcavity). One intriguing prediction of this model is the existence of a family of slow photonic modes occupying the boundary of the first Brillouin zone.

1.2   General properties of exciton polaritons

Before going into details, however, let us try to deduce the features of the polaritonic bandstructure based on general physical arguments.

First, imagine turning off the interaction between the dipoles and the electromagnetic field. The system now contains two independent elementary ex-
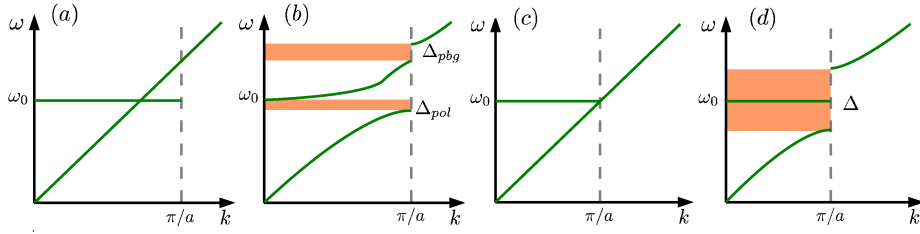
Figure 1.1: Sketch of polaritonic dispersion relation for (a) detuned lattice with no electromagnetic interaction, (b) detuned lattice with interaction, (c) tuned lattice with no interaction, and (d) tuned lattice with interaction. The exciton frequency is $\omega = \omega_0$, and $k = \pi/a$ is the boundary of the first Brillouin zone.

citations: (i) free electromagnetic waves with dispersion relation $\omega = ck$, and (ii) free dipoles oscillations at the resonant frequency ω_0. These dispersion relations are sketched in Fig. 1.1(a) for a detuned lattice ($\omega_0 \neq c\pi/a$, where a is the lattice spacing), and in Fig. 1.1(c) for a tuned lattice ($\omega_0 = c\pi/a$). The dipole dispersion relation terminates at the Brillouin zone boundary $k = \pi/a$, which, as we shall see, corresponds to the fact that the dipoles form a discrete lattice and not a continuum.

When we turn on the interaction between the dipoles and the electromagnetic field, the elementary excitations are polaritons, i.e. mixtures of electromagnetic waves and dipole oscillations. For the detuned lattice, we can guess what the polaritonic dispersion relation looks like: as shown in Fig. 1.1(b), a polaritonic band gap Δ_{pol} appears at $\omega = \omega_0$, because the field-dipole coupling is strongest when their frequencies match; and a photonic band gap appears at $k = \pi/a$, where Bragg scattering is most pronounced.

The polariton dispersion relation naturally splits into three distinct bands (more if you count higher Brillouin zone boundaries, which we'll ignore).

When we tune the lattice, the two band gaps merge into a single gap, as shown in Fig. 1.1(d). The mutual repulsion between the bands "squeezes" the middle band, reducing its group velocity to zero. This is the family of slow longitudinal modes seen by Deutsch *et. al.* and other authors.

The actual polaritonic bandstructure has certain other features that are not so easy to deduce. For instance, we will see that the combined bandgap in the tuned lattice is much larger than the sum of the detuned lattice's photonic and polaritonic bandgaps. Also, although the "squeezed" middle branch of polaritons has vanishing group velocity, at $k = \pi/a$ it consists entirely of free electromagnetic waves, with no dipole oscillations. In higher dimensions, these "Bragg resonant" modes generalize to a family of modes occupying the entire boundary of the first Brillouin zone. The theory that I will now present describes these effects quantitatively.

1.3   Model Hamiltonian

Consider N localized atoms of the same type in a 3D cubic lattice, at sites $\vec{r}_i$ with lattice period ℓ. The lattice is fully filled, with exactly one atom at each site (i.e., an $n = 1$ Mott insulator). To facilitate calculation, we enclose the lattice in a periodic electromagnetic cavity of volume V, which reproduces the physical behavior inside a sufficiently large lattice. The Coulomb-gauge

Hamiltonian is

$$H = \sum_i H_i + \sum_{\vec{k}\sigma} \hbar c |\vec{k}| \, a_{\vec{k}\sigma}^\dagger a_{\vec{k}\sigma} - \frac{e}{mc} \sum_i \vec{A}(\vec{r}_i) \cdot \vec{p}_i. \qquad (1.1)$$

Here, H_i is the Hamiltonian for the valence electron on the i-th atom, and $\vec{p}_i$ is its momentum operator. $a_{\vec{k}\sigma}^\dagger$ and $a_{\vec{k}\sigma}$ are creation and annihilation operators for photons with wavevector $\vec{k}$ and linear polarization σ. $\vec{A}(\vec{r})$ is the vector potential,

$$\vec{A}(\vec{r}) = \sum_{\vec{k}\sigma} \sqrt{\frac{2\pi\hbar c}{V|\vec{k}|}} \left(a_{\vec{k}\sigma} \, e^{i\vec{k}\cdot\vec{r}} + a_{\vec{k}\sigma}^\dagger \, e^{-i\vec{k}\cdot\vec{r}} \right) \hat{e}_{\vec{k}\sigma}, \qquad (1.2)$$

where $\hat{e}_{\vec{k}\sigma}$ is the unit polarization vector for $a_{\vec{k}\sigma}^\dagger$.

Let us suppose that the photon polarizations (two for each value of $\vec{k}$) excite orthogonal atomic states. If the number of excited atoms is much smaller than N, the photon polarizations decouple, and we can drop the σ label in (1.1), subject to the understanding that we are working with a specific polarization for each $\vec{k}$. This is consistent with the weak polarization dependence obtained by van Coevorden *et. al.*[12] In contrast, polarization effects play an important role in solid-state resonant photonic crystals[8–11], due to the finite size of the scattering centers.

The atomic Hamiltonian now reduces to that of a two-level system,

$$H_i = \epsilon \, b_i^\dagger b_i, \qquad (1.3)$$

where ϵ is the energy difference between the atomic levels, and $b_i^\dagger \equiv |1\rangle\langle 0|_i$ and $b_i \equiv |0\rangle\langle 1|_i$ are the atomic level raising and lowering operators. We will refer to the particle-like entities created by the atomic raising operator $b_i^\dagger$ as Frenkel excitons, or simply as "excitons".

Given that the electronic wavefunctions are typically much narrower than the lattice spacing, we can treat the $\vec{r}_i$ in (1.1) as numbers (perfect lattice positions) rather than operators. At each site, the momentum operator is

$$\vec{p}_i = \frac{i}{\hbar}\,m\epsilon\,\vec{x}_{01}(b_i^\dagger - b_i)\,,\quad \vec{x}_{01} \equiv \langle 1|\vec{x}|0\rangle. \tag{1.4}$$

Let us also define momentum-space exciton operators

$$\begin{aligned}
b_{\vec{q}} &= \frac{1}{\sqrt{N}}\sum_i e^{-i\vec{q}\cdot\vec{r}_i}\,b_i \\
b_{\vec{q}}^\dagger &= \frac{1}{\sqrt{N}}\sum_i e^{i\vec{q}\cdot\vec{r}_i}\,b_i^\dagger,
\end{aligned} \tag{1.5}$$

where the wavevectors $\vec{q}$ are restricted to the first Brillouin zone, corresponding to the fact that an exciton has no physical meaning between lattice points.

The momentum-space exciton operators obey the following commutation relations:

$$[b_{\vec{q}}, b_{\vec{q}'}^\dagger] = \delta_{\vec{q}\vec{q}'} + O(M/N), \tag{1.6}$$

where M is the number of excited atoms. We have already assumed that $M < N$. Thus, the excitons can be approximately treated as bosons[20]. (This is similar to the argument for treating spin waves as bosons.)

Substituting (1.2)-(1.5) into (1.1), we obtain the microscopic polariton Hamiltonian first derived by Hopfield[20] in the context of crystalline solids:

$$
H = \sum_{\vec{q}} \left\{ \epsilon\, b_{\vec{q}}^{\dagger} b_{\vec{q}} + \sum_{\vec{G}} \hbar c\, |\vec{q} + \vec{G}|\, a_{\vec{q}+\vec{G}}^{\dagger} a_{\vec{q}+\vec{G}} \right.
$$

$$
- \sum_{\vec{G}} i\, C_{\vec{q}+\vec{G}} \left[\left(b_{\vec{q}}^{\dagger} a_{\vec{q}+\vec{G}} - a_{\vec{q}+\vec{G}}^{\dagger} b_{\vec{q}} \right) \right.
$$

$$
\left. \left. + \left(b_{\vec{q}}^{\dagger} a_{-(\vec{q}+\vec{G})}^{\dagger} - a_{-(\vec{q}+\vec{G})} b_{\vec{q}} \right) \right] \right\}, \quad (1.7)
$$

where $\vec{G}$'s run over all reciprocal lattice vectors, and

$$
C_{\vec{q}+\vec{G}} = \sqrt{\frac{2\pi\alpha N}{|\vec{q} + \vec{G}|\, V}}\, \epsilon\, x_{01}, \qquad (1.8)
$$

where α is the fine-structure constant.

The atom-photon interaction consists of two parts. The first part, on the second line of (1.7), describes the lattice absorbing a photon with wavevector $\vec{q} + \vec{G}$ to create an exciton with wavevector $\vec{q}$, and the reverse process of destroying an exciton to emit a photon. The remaining interaction terms describe the creation and annihilation of associated pairs of photons and excitons. The usual way to diagonalize (1.7) is to introduce polariton operators $\alpha_{\vec{q}}$[20,23] for each reduced wavevector $\vec{q}$, as linear combinations of $b_{\vec{q}}$, $b_{-\vec{q}}^{\dagger}$, $a_{\vec{q}+\vec{G}}$, and $a_{-\vec{q}+\vec{G}}^{\dagger}$ (for all $\vec{G}$). Stipulating that these act as decoupled lowering operators for H, one obtains the polariton energies as solutions of a $(2n + 1) \times (2n + 1)$ eigenvalue problem for each $\vec{q}$, where n is the number

of Brillouin zones included in the calculation. Higher Brillouin zones were first included into the Hopfield theory by Knoester and Mukamel[23] in their calculation of polariton-mediated intermolecular forces in solids. There, the photons in the higher Brillouin zones were taken to be decoupled from the excitons, which was appropriate since the Brillouin zone energy was many orders of magnitude larger than ϵ. In our system, the two energies are comparable, and we must incorporate the interaction up to at least the second-order zones.

It simplifies the calculations to drop the "counter-rotating" interaction terms in (1.7) describing the creation and annihilation of pairs. This is physically justifiable even though the discarded terms have the same coupling strength $C_{\vec{q}+\vec{G}}$ as the remaining interaction terms, because the pair creation and annihilation process is a quantum mechanical fluctuation of the "vacuum" with a finite energy gap $\epsilon + \hbar c|\vec{q}|$. For ϵ and $\hbar c|\vec{q}|$ both on the order of eV, and lattice periods at optical wavelengths, $C_{\vec{q}} \sim 10^{-4}\,\text{eV} \ll \epsilon + \hbar c|\vec{q}|$. Such fluctuations are thus extremely rare and have a negligible effect on particle energies. The interaction terms describing the conversion of a real photon into an exciton, and vice versa, remain important: since the existing particle possesses energy, these processes involve a much smaller energy fluctuation. The approximation holds provided we look at values of $|\vec{q}|$ comparable to both $\epsilon/\hbar c$ and the Brillouin zone energy, which is exactly the regime we are interested in.

The Hamiltonian now decouples into N independent pieces, one for each

reduced wavevector:

$$H = \sum_{\vec{q}} H_{\vec{q}}, \tag{1.9}$$

where

$$
\begin{aligned}
H_{\vec{q}} &= \epsilon\, b_{\vec{q}}^\dagger b_{\vec{q}} + \sum_{\vec{G}} \hbar c \, |\vec{q} + \vec{G}| \, a_{\vec{q}+\vec{G}}^\dagger a_{\vec{q}+\vec{G}} \\
&\quad - \sum_{\vec{G}} i\, C_{\vec{q}+\vec{G}} \left(b_{\vec{q}}^\dagger a_{\vec{q}+\vec{G}} - a_{\vec{q}+\vec{G}}^\dagger b_{\vec{q}} \right).
\end{aligned} \tag{1.10}
$$

This says that each photon mixes with all other photons having wavevectors that differ by a reciprocal lattice vector, as one expects of a Photonic Crystal system. Here, the mixing is mediated by the atom-photon interaction. Since (1.10) has the quadratic form $\sum_{ij} \beta_i^\dagger \mathcal{H}_{ij} \beta_j$, it can be diagonalized as $\sum_n E_n \alpha_n^\dagger \alpha_n$, where the α's are boson operators defined by $\alpha_n = \sum_j w_j^{*n} \beta_j$, E_n is the nth eigenvalue of $\mathcal{H}$, and w^n is the corresponding eigenvector. Therefore, we can obtain the polariton energies $E_{\vec{q}}^n$ by including a finite number of Brillouin zones in the sum and diagonalizing the associated matrix.

1.4   Band structure

Fig. 1.2 shows the polariton dispersion curves along the [100] direction for a blue-detuned optical lattice. The interaction opens up two energy gaps in the polariton spectrum: an indirect "polaritonic gap" Δ_{pol} at ϵ due to the repulsion between the bare dispersion curves, and a photonic band gap Δ_{pbg}
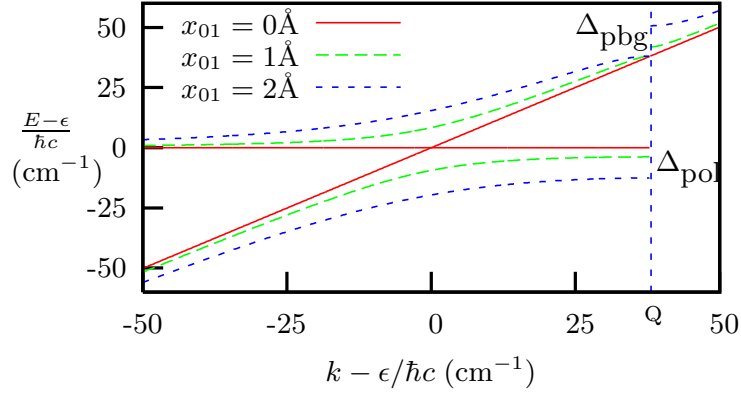
Figure 1.2: Single-polariton dispersion for a 3D cubic lattice along [100] in the extended zone scheme, with $\epsilon = 3\,\text{eV}$ and three different coupling strengths, associated with the parameters $x_{01} = 0$ (non-interacting), $1\,\text{Å}\,(C_Q \sim 0.18\,\text{meV})$, and $2\,\text{Å}\,(C_Q \sim 0.35\,\text{meV})$. The vertical dashed line indicates the Brillouin zone boundary at $|\vec{Q}| = 1.00025\,\epsilon/\hbar c$. The graphs are generated numerically from (1.10), summing over 125 Brillouin zones.

at $\hbar c|\vec{Q}|$ where $\vec{Q}$ is the Brillouin zone boundary. We have also calculated the density of polariton states; after integrating over all angles, we find that the density of states is enhanced near the band edges, but remains nonzero at all energies because the exact sizes and positions of the gaps vary with angle. The system therefore does not possess a complete gap, essentially because of the weakness of the electromagnetic interaction. The gap sizes vary continuously as we change the lattice period a, and thus V (keeping N and all other parameters constant). As shown in Fig. 1.3, the gaps meet and become significantly enhanced when the Brillouin zone boundary intersects the crossing point of the bare dispersion curves.

To understand the nature of the spectrum at the Brillouin zone boundary,

consider a photon with wavevector $\vec{k} = \vec{Q}$ along one of the faces of the cube. There is another such photon, with wavevector $\vec{Q} + \vec{G}'$ lying on the opposite face, such that $|\vec{Q}| = |\vec{Q} + \vec{G}'|$. (When $\vec{Q}$ lies on an edge or corner of the Brillouin zone boundary, there are more partners; we will not consider these cases, but they can be treated in a similar fashion.) The two photons mix strongly since they have the same energy, so we can neglect the other photon states and use the effective Hamiltonian

$$
\tilde{H}_{\vec{Q}} = \begin{bmatrix} b_{\vec{Q}} \\ a_{\vec{Q}} \\ a_{\vec{Q}+\vec{G}'} \end{bmatrix}^{\dagger} \begin{bmatrix} \epsilon & -iC_{\vec{Q}} & -iC_{\vec{Q}} \\ iC_{\vec{Q}} & \hbar c|\vec{Q}| & 0 \\ iC_{\vec{Q}} & 0 & \hbar c|\vec{Q}| \end{bmatrix} \begin{bmatrix} b_{\vec{Q}} \\ a_{\vec{Q}} \\ a_{\vec{Q}+\vec{G}'} \end{bmatrix}. \tag{1.11}
$$

Thus, the polariton energies at the Brillouin zone boundary are

$$
\begin{aligned}
E_{\vec{Q}}^{0} &= \hbar c|\vec{Q}|, \\
E_{\vec{Q}}^{\pm} &= \frac{\epsilon + \hbar c|\vec{Q}|}{2} \pm \sqrt{\left(\frac{\epsilon - \hbar c|\vec{Q}|}{2}\right)^{2} + 2C_{\vec{Q}}^{2}} \,.
\end{aligned} \tag{1.12}
$$

These are exactly the energy levels resulting from Rabi splitting of a two-level atom interacting with two counterpropagating photon states with wavevectors $\pm\vec{Q}$, with an effective cavity size V/N. In the exactly-tuned case $\epsilon = \hbar c|\vec{Q}|$, $E_{\vec{Q}}^{\pm}$ has a special significance: as shown in Fig. 1.3(b), these are the upper and lower edges of the band gap. The resonant enhancement of the band gap in this system is thus a manifestation of the Purcell effect[13]. Intuitively, we can imagine enclosing a single atom in a microcavity with the
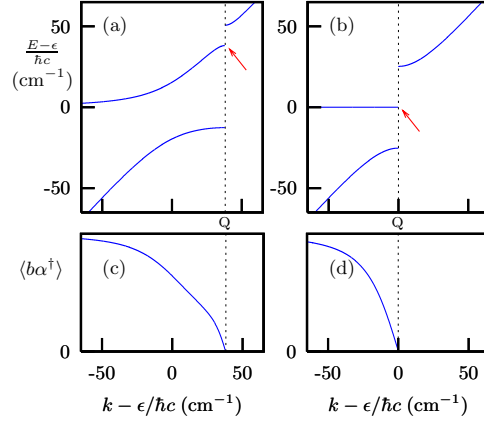
Figure 1.3: Single-polariton dispersion along [100], with $\epsilon = 3\,\mathrm{eV}$, $x_{01} = 2\,\mathrm{Å}$, and different lattice periods: (a) $|\vec{Q}| = 1.00025\,\epsilon/\hbar c$, and (b) $|\vec{Q}| = \epsilon/\hbar c$. Plots (c) and (d) show the corresponding overlaps of the polariton with the bare exciton, $\langle 0| b_{\vec{q}}\alpha^{\dagger}_{\vec{q}}|0\rangle$, for the polaritons on the dispersion curve leading to the purely photonic state at $\vec{q} = \vec{Q}$ (indicated with arrows in (a) and (b)), which have no atomic component.

dimensions of the unit cell; if the cavity walls are mirrors, the atom sees a lattice of atoms similar to the one considered here.

We have checked (1.12) against numerical solutions of (1.10) including the 125 lowest Brillouin zones, for various values of $\vec{Q}$ along the Brillouin zone boundary up to $40°$ from the [100] direction. For $\epsilon = 3\,\mathrm{eV}$ and $x_{01} = 2\,\mathrm{Å}$, the error is always less than $0.02\,\mathrm{cm}^{-1}$, three orders of magnitude smaller than the maximum gap size.

The size of the gaps in the exactly-tuned limit can be estimated by substituting $\epsilon = \hbar c|\vec{Q}'|$ into (1.12):

$$\Delta \approx \sqrt{2}\, C'_{\epsilon/\hbar c} = \sqrt{\frac{4\alpha x_{01}^2 \epsilon^4}{\pi^2(\hbar c)^2}}. \tag{1.13}$$

For $\epsilon, \hbar c |\vec{Q}| \approx 3\,\mathrm{eV}$, and $x_{01} \approx 2\,\text{Å}$, $\Delta/\hbar c \approx 25\,\mathrm{cm}^{-1}$ ($\sim 10^{-4}\,\epsilon$), in agreement with Fig. 1.3(b). We can also obtain limiting expressions for the gaps when they are significantly decoupled. Consider $|\vec{Q}| > \epsilon/\hbar c$, as in Fig. 1.3(a). Away from the Brillouin zone boundary, we can neglect the effect of photons in higher Brillouin zones, and the effective Hamiltonian matrix is $\mathcal{H} = [\, \epsilon, \, -iC_{\vec{q}}; \, iC_{\vec{q}}, \, \hbar c |\vec{q}| \,]$, with eigenvalues

$$E_{\vec{q}}^{\pm} = \frac{\epsilon + \hbar c |\vec{q}|}{2} \pm \sqrt{\left(\frac{\epsilon - \hbar c |\vec{q}|}{2}\right)^2 + C_{\vec{q}}^2} \,. \tag{1.14}$$

The contribution to the indirect polaritonic gap from the large-q branch of the dispersion curve, which is truncated at the Brillouin zone boundary, is obtained from the large-q expansion of (1.14) evaluated at $\vec{q} = \vec{Q}$. The contribution from the small-q branch cannot be found by setting $\vec{q} = 0$ in (1.14) due to our preceding approximations, so we instead calculate an upper bound on it by evaluating it at the minimum, $|\vec{q}| = \epsilon/2\hbar c$. The resulting polaritonic gap is

$$\Delta'_{\mathrm{pol}} \simeq \frac{4C_{\epsilon/\hbar c}^2}{\epsilon} + \frac{C_{\vec{Q}}^2}{\hbar c Q} \tag{1.15}$$

With the same lattice parameters, $\Delta'_{\mathrm{pol}} \approx 10^{-3}\,\mathrm{cm}^{-1}$ ($\sim 10^{-8}\,\epsilon$). From the large-$|\vec{Q}|$ expansion of (1.12), the photonic band gap is $\Delta'_{\mathrm{pbg}} = C_{\vec{Q}}^2/\hbar c |\vec{Q}|$, strictly smaller than (1.15). Therefore, the effects of the polaritonic interaction are very small when the system is detuned.

This model can also be used to study the quasi-1D geometry considered by many authors, in which atoms are trapped along periodically-stacked

infinite sheets. Consider a 3D lattice in which the lattice spacing in one of the directions, ℓ_1, is much larger than the spacing in the other two directions. The relevant wavevectors, lying on the Brillouin zone boundaries closest to the origin, have magnitude $|\vec{Q}_1| = \pi/\ell_1$ and point in the direction of stacking. In this regime, this model can be directly compared with the semiclassical analysis of Deutsch *et. al.*[7]. For instance, the semiclassical theory predicts band gaps from $E_-^{(cl)}$ to ϵ and from $\hbar c|\vec{Q}_1|$ to $E_+^{(cl)}$ for blue-detuned lattices. A short calculation, using Eq. 15-19 of that paper, yields

$$E_\pm^{(cl)} \approx \frac{\epsilon + \hbar c|\vec{Q}|}{2} \pm \sqrt{\left(\frac{\epsilon - \hbar c|\vec{Q}|}{2}\right)^2 + 2 \cdot \frac{3\hbar^2 c\gamma\eta}{2|\vec{Q}_1|}} \qquad (1.16)$$

where η is the surface density along each sheet and $\gamma \ll (E_\pm - \epsilon)/\hbar$ is the linewidth of the atomic transition. Using the golden rule prescription for the natural linewidth[24], $\gamma = (4\alpha\epsilon^3 x_{01}^2)/(3\hbar^3 c^2)$, this reduces to (1.12) with C_Q^2 replaced by $C_Q^2 \cdot \epsilon/\hbar c|\vec{Q}_1|$. The band gaps predicted by the semiclassical and quantum mechanical theories are thus similar for $\epsilon \sim \hbar c|\vec{Q}_1|$, which is also the regime where the band gaps are significant. In the exactly-tuned case, the results are identical, and one obtains

$$\Delta_{1d} = 2\epsilon x_{01}\sqrt{\alpha\eta}\,. \qquad (1.17)$$

Actual 1D/2D lattices are more problematic since each exciton is coupled to photons with a continuum of wavenumbers in the transverse direction,

which smears out the gaps. One might avoid this using an actual cavity in the transverse direction, making the electromagnetic field effectively 1D/2D.

1.5 Slow polariton modes

The energy E_Q^0 in (1.12) corresponds to a polariton created by the operator $(a_Q^\dagger - a_{Q+G'}^\dagger)/\sqrt{2}$. This remains an exact polariton state when we include higher Brillouin zones in the effective Hamiltonian. (In fact, there is a family of such states for each pair of Brillouin zone boundaries.) These "purely photonic" polaritons are reminiscent of "dark states" in electromagnetically induced transparency (EIT)[14], since (1.11) is identical to the EIT effective Hamiltonian with the exciton and two photon modes acting as the levels of the Λ system. In EIT, a "dark state" arises: a coherent superposition of atomic levels that does not couple to the radiation. The analog in our case is a non-interacting photonic state, with no atomic component. Its classical limit is a standing electromagnetic wave commensurate with the lattice. Since the laser light that supports the lattice always falls exactly on the Brillouin zone boundary[7], the stability of the optical lattice relies on the existence of such standing wave modes; other modes are Bragg reflected away. In a sense, the lattice "selects" the standing wave modes from the incoming laser light. Similar modes have been observed in other resonant photonic crystal systems[9–11]. We have shown here that in the self-consistent limit of complete quantum coherence and low exciton density, this selection
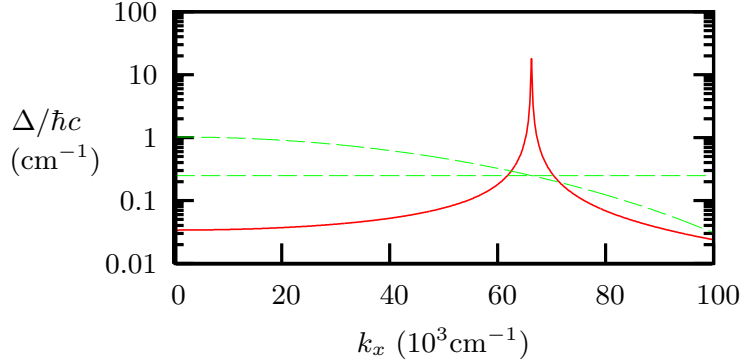
Figure 1.4: Photonic gap at wavevectors $\vec{Q} = [k_x, \pi/\ell, 0]$ along the Brillouin zone boundary, for $\epsilon = 3\,\mathrm{eV}$, $x_{01} = 2\,\mathrm{\mathring{A}}$, and $\pi/\ell = 0.9\,\epsilon/\hbar c = 1.4 \times 10^5\,\mathrm{cm}^{-1}$ (red-detuned). The dashed lines show k_y vs. k_x for the surface $|\vec{k}| = \epsilon/\hbar c$ and the Brillouin zone boundary; here, the ordinate is not drawn to scale. The gap is largest at the intersection of the two surfaces, i.e. $|\vec{Q}| = \epsilon/\hbar c$.

takes place at the quantum state level. Only the purely photonic polaritons can support a macroscopic population, since they are the only elementary excitations of the interacting system with zero atomic component.

In the 3D system, there is a family of purely photonic polaritons everywhere on the boundary of the first Brillouin zone. Remarkably, these states are attached to the slow, "atomic" branch of the dispersion curve. These appear to be analogs of the slow, non-degenerate, longitudinal electromagnetic modes that appear in the classical t-matrix calculation of Coevorden *et. al.*[12] Our model shows that the photonic component along this branch goes continuously from nearly zero to unity as we approach the Brillouin zone boundary, as shown in Fig. 1.3(c) and (d). Therefore, by exciting polaritons

over a range

$$\left| \frac{\epsilon - \hbar c |\vec{Q}|}{\hbar c} \right| \sim \frac{C_{\vec{Q}}}{\hbar c} \sim 10 \, \text{cm}^{-1} \tag{1.18}$$

around wavevector $\vec{Q}$, one could create a wavepacket that propagates slowly but has low exciton density.

1.6 Conclusions

According to the simple model presented in the preceding sections, we see that the laser light supporting an optical lattice is allowed to fill the lattice, despite the phenomenon of Bragg reflection, due to the nature of the optical lattice as a resonant photonic crystal. This conclusion is in agreement with the findings of Deutsch *et. al.*[7], but applies to three dimensions and the fully quantum mechanical regime.

In modern optical lattices, the trapping beams are usually set far-detuned from optical resonance. However, it should be possible to study nearly-tuned systems, such as alkali atoms loaded in a cubic lattice made by near-IR light. In that case, the present model predicts an unusually large bandgap containing a slow-light mode, which could be probed by introducing a probe beam at an angle to the axis of the lattice. One should choose an atomic transition ϵ such that $1 \leq \epsilon \ell / \pi \hbar c \leq \sqrt{3}$, where ℓ is the lattice period, and use probe wavevectors with magnitude lying in a range $\Delta / \hbar c \sim 10 \, \text{cm}^{-1}$ around $|\vec{q}| = \epsilon / \hbar c$, at an angle $\cos^{-1}(\pi \hbar c / \epsilon \ell)$ to a lattice axis (Fig. 1.4). Although the present theory applies to an infinite lattice, the predicted frequency shifts

may be observable close to the atomic resonance, even in a lattice of about 100 atoms on a side.

We have treated the atomic positions as fixed, as would be the case for a strongly-confining optical lattice where the rate at which each atom tunnels to a different lattice site is negligible compared to the radiative lifetime. The presence of non-zero hopping amplitudes would add an imaginary part to the polariton energies, proportional to the tunneling rate. The size of the band gaps would be reduced by the corresponding amount.

Chapter 2

Band theory of dark-state polaritons

2.1 Dark-state polaritons

Several years ago, Fleischhauer and Lukin[15] predicted the existence of a stable polaritonic excitation in Λ-type media [Fig. 2.1(a)] exhibiting electromagnetically induced transparency (EIT)[14]. This is a coherent quantum excitation whose evolution is governed by a classical control field; because it involves a vanishing population of excited states, it was dubbed the "darkstate polariton". The dark state polariton concept has been used in remarkable experiments that manipulate the motion of single photons, including "stopping light"[25,26].

---

*Y. D. Chong and M. Soljačić, Phys. Rev. A **77**, 013823 (2008).

37
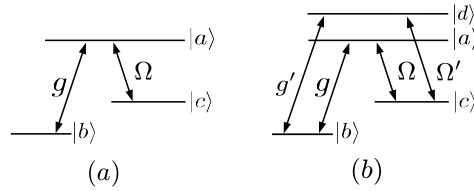
Figure 2.1: (a) 3-level Λ-type medium. (b) Double-Λ medium.

The original Fleischhauer-Lukin result was derived as a perturbation expansion of the field operator equations of motion in the limit of strong control fields. In a subsequent work, Juzeliūnas and Carmichael[27] used a Bogoliubov-type transformation to diagonalize the model Hamiltonian exactly, and showed that the dark-state polariton can be understood as a part of a branch of slow polaritons occurring in systems containing a pair of atomic resonances. These authors also emphasized the fact that the photonic part of the polariton mixes with atomic excitations possessing wavevectors differing by the wavevector of the control field. Thus, for instance, it is possible to reverse the direction of a polariton wavepacket by switching the direction of the control field.

In this chapter, I present a derivation of the dark-state polariton using the Sawada-Brout technique[28]. This approach allows us to understand the properties of the dark-state polariton in terms of band theory, in the same spirit as the analysis of exciton polaritons in the previous chapter. In a sense, this chapter serves as a generalization of the exciton polariton concept from two-level atoms to Λ-type atoms. The present approach can also be thought of as a simplified version of the method used by Juzeliūnas and

Carmichael. We shall see how the band-theoretical model reduces to the model of Fleischhauer and Lukin, a result that was not demonstrated by Juzeliūnas and Carmichael[27].

We will also see how the analysis can be extended to a double-Λ medium, shown in Fig. 2.1(b). Such a medium contains a dark-state polariton consisting of low-lying atomic excitations and photon states of two different frequencies[29,30].

In both single- and double-Λ systems, the dark-state polariton is protected against incoherent decay processes acting on the excited states, because it contains a vanishing population of these states. It has previously been shown that double-Λ media can efficiently upconvert classical probe beams[31,32], and a related four-wave mixing scheme has already been used in such systems to generate correlated photon pairs[33–36]. We will explore the possibility of exploiting the dark-state polariton to perform single-photon frequency conversion in a manner that preserves quantum coherence. Unlike semiclassical analyses in which the electromagnetic field is treated classically[31,32], this theory applies to the single-photon regime. It may thus have applications in quantum information processing, such as for downconverting a member of an entangled photon pair to a frequency suitable for transmission over a telecommunications fiber. Unlike parametric conversion schemes exploiting optical nonlinearities, the relevant photons are up- or down-converted individually, instead of being split or recombined; the additional momentum and energy are supplied by the control fields.

2.2   Single-Λ system

We begin by considering an N-atom gas with a single-Λ level structure, shown in Fig. 2.1(a). The ground, excited, and metastable atomic states are respectively denoted by $|b\rangle$, $|a\rangle$, and $|c\rangle$, and their corresponding energies by $\hbar\omega_b$, $\hbar\omega_a$, and $\hbar\omega_c$. The atomic Hamiltonian is

$$H_0 = \hbar \sum_r \left(\omega_a \sigma_r^{aa} + \omega_b \sigma_r^{bb} + \omega_c \sigma_r^{cc} \right), \tag{2.1}$$

with the sum performed over all atomic positions r. Here,

$$\sigma_r^{\mu\nu} \equiv |\mu\rangle_r \langle\nu|_r \tag{2.2}$$

denotes a transition operator for the atom at position r. We also define Fourier-transformed operators, $\sigma_k^{ab} \equiv N^{-1/2} \sum_r \sigma_r^{ab} e^{ikr}$ etc. The photon Hamiltonian is

$$H_1 = \sum_k \hbar c |k| a_k^\dagger a_k, \tag{2.3}$$

where $a_k^\dagger$ and a_k are photon creation and destruction operators. The photons interact with the ab transition through the minimal-coupling Hamiltonian

$$H_2 = -\hbar g \sum_k a_k \, \sigma_k^{ab} + \text{h.c.} \tag{2.4}$$

The coupling constant is $g \simeq \mathcal{P}\sqrt{2\pi N \omega_{ab}/\hbar V}$, where $\mathcal{P}$ is the dipole moment of the ab transition, $\omega_{ab} \equiv \omega_a - \omega_b$, and V is the cavity volume. For notational

simplicity, we have used the rotating-wave approximation. Finally, we include a classical control field with strength (Rabi frequency) Ω, frequency $\omega_L \sim \omega_{ac}$, and wavevector k_L:

$$H_3(t) = -\hbar\Omega\, e^{-i\omega_L t} \sum_r e^{ik_L r}\, \sigma_r^{ac} + \text{h.c.} \qquad (2.5)$$

Here, we have again discarded counter-rotating terms. We neglect the coupling between the photons and the ac transition, which is negligible compared to the effects of the control field, and the coupling between the control field and the ab transition, which is off resonance.

The time dependence in (2.5) can be removed by defining

$$H_L = U_L(t)H(t)U_L^\dagger(t) + \hbar\omega_L \sum_r \sigma_r^{cc}, \qquad (2.6)$$

where $H(t) \equiv H_0 + \cdots + H_3(t)$, and

$$U_L(t) = \exp\left[-i\omega_L t \sum_r \sigma_r^{cc}\right]. \qquad (2.7)$$

The Schrödinger equation $H(t)\,|\psi(t)\rangle = i\hbar\partial_t\,|\psi\rangle$ can be then rewritten as

$$i\hbar\frac{\partial}{\partial t}\left[U_L(t)\,|\psi(t)\rangle\right] = H_L\left[U_L(t)\,|\psi(t)\rangle\right]. \qquad (2.8)$$

Thus, we can extract solutions to the Schrödinger equation from the energy eigenstates of the time-independent Hamiltonian H_L. To obtain these, we

look for a polariton excitation operator $A^\dagger$ such that

$$[H_L, A^\dagger] = \hbar\omega A^\dagger + \cdots \tag{2.9}$$

The polariton is long-lived provided the omitted terms are negligible[28]. If the initial state of the system is its (zero photon) ground state, $A^\dagger$ should be a mixture of $a^\dagger$, σ^{ab}, and σ^{cb}.

The commutation relations of these three operators with H_L are listed below. We have removed terms involving σ^{ba}, σ^{aa}, σ^{ca}, and a_k; since these operators give zero when acting on the ground state, this introduces no additional error for single-polariton excitations. Similarly, we have replaced σ_k^{bb} with $\sqrt{N}\delta_{k0}$. Thus,

$$\left[H_L, \sigma_k^{ab}\right] \simeq \hbar\omega_{ab}\sigma_k^{ab} - \hbar\Omega^* \sigma_{k-k_L}^{cb} - \hbar g^* a_k^\dagger \tag{2.10}$$

$$\left[H_L, \sigma_{k-k_L}^{cb}\right] \simeq \hbar(\omega_{cb} + \omega_L)\sigma_{k-k_L}^{cb} - \hbar\Omega\, \sigma_k^{ab} \tag{2.11}$$

$$[H_L, a_k^\dagger] = \hbar c|k|a_k^\dagger - \hbar g\, \sigma_k^{ab}. \tag{2.12}$$

Let us now look for excitation operators of the form

$$A_{nk}^\dagger = -\phi_{nk}^1\, \sigma_k^{ab} + \phi_{nk}^2\, \sigma_{k-k_L}^{cb} + \phi_{nk}^3\, a_k^\dagger, \tag{2.13}$$

where the band index n enumerates the different polariton species. The c-numbers ϕ_{nk}^j are determined by inserting (2.13) into (2.9) and using (2.10)-
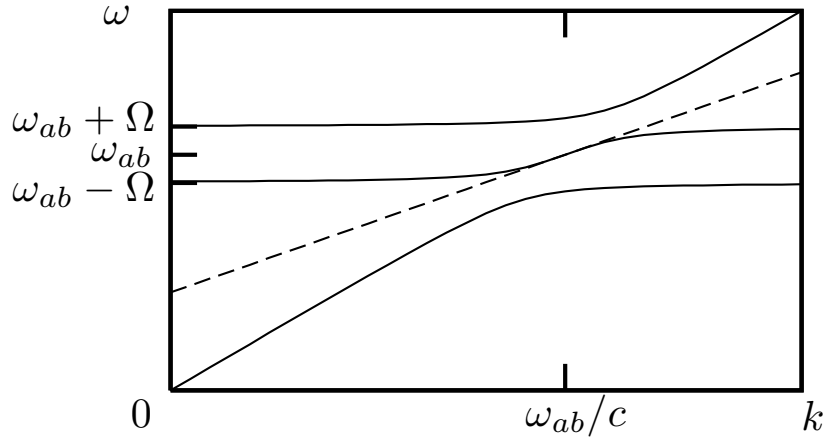
Figure 2.2: Polaritonic dispersion curve for $\omega_L = \omega_{ac}$. The solid lines show the exact polariton solutions given by Eq. (2.14); the dashed line showss the Fleischhauer-Lukin solution, Eq. (2.16).

(2.12). This gives three self-consistency equations that can be written as

$$
\begin{bmatrix}
\omega_{ab} & \Omega & g \\
\Omega^* & \omega_{cb} + \omega_L & 0 \\
g^* & 0 & c|k|
\end{bmatrix}
\begin{bmatrix}
\phi^1 \\
\phi^2 \\
\phi^3
\end{bmatrix}_{nk}
= \omega_{nk}
\begin{bmatrix}
\phi^1 \\
\phi^2 \\
\phi^3
\end{bmatrix}_{nk}
. \tag{2.14}
$$

The form of the effective Hamiltonian in (2.14) is familiar from semiclassical analyses of EIT. Fig. 2.2 shows the bandstructure in the absence of loss, similar to the one obtained by Juzeliūnas and Carmichael[27]. For simplicity, let us assume that $\omega_L = \omega_{ac}$. The asymptotic eigenfrequencies far from resonance are $c|k|$ and the eigenvalues of the upper-left 2×2 submatrix in the effective Hamiltonian, in this case $\omega_{ab} \pm \Omega$. Exactly at resonance

$(|k| = \omega_{ab}/c)$, there is an eigenvector

$$\begin{bmatrix} \phi^1 \\ \phi^2 \\ \phi^3 \end{bmatrix}_{\text{DSP}} \propto \begin{bmatrix} 0 \\ 1 \\ -\Omega/g \end{bmatrix}. \qquad (2.15)$$

For slightly detuned k, this continues into eigenvectors where the σ^{ab} component is nonzero but small. These solutions—"dark-state polaritons"—are thus insensitive to incoherent decay processes acting on $|a\rangle$.

The stability of the exactly-resonant dark-state polariton is limited only by the lifetime of the metastable state $|c\rangle$, which we shall assume to be longer than the time-scale of any relevant experiment. For off-resonant dark-state polaritons, the decay rate is only quadratic in the detuning: upon replacing ω_a with $\omega_a - i\Gamma_a$ in (2.14), one finds that the imaginary part acquired by ω_k is $\sim \Gamma_a |\Delta/\Omega|^2$ (for $\Omega \gg g$), where $\Delta \equiv c|k| - \omega_{ab}$. The other two polariton branches correspond to "bright" polaritons that contain significant $|a\rangle$ population and are thus strongly affected by losses. Like Fleischhauer and Lukin[15], we neglect Langevin noise effects, which do not influence the adiabatic evolution of the dark-state polaritons.

Expanding around $\omega = \omega_{ab}$ yields a limiting solution for the dark-state polaritons:

$$\omega_k = \omega_{ab} + \frac{|\Omega|^2}{|g|^2 + |\Omega|^2} \left(c|k| - \omega_{ab} \right) \qquad (2.16)$$

$$\phi_k^1 = \frac{\Omega(c|k| - \omega_{ab})}{|g|^2 + |\Omega|^2} \phi_k^2 \tag{2.17}$$

$$\phi_k^3 = -\frac{\Omega}{g} \phi_k^2. \tag{2.18}$$

Equations (2.16)-(2.18) agree with the solution derived by Fleischhauer and Lukin using a perturbation expansion in $1/\Omega^{15}$. In the present formalism, the fact that decreasing Ω reduces the polaritonic group velocity can be intuitively understood as the result of "squeezing" the bandwidth of the middle polariton band. An interesting property of the dark-state polariton solution is that it does not depend on the energies of the underlying Λ system, only the detuning of the control field and the coupling parameters g and Ω.

Finally, we can extract the solutions to the original Schrödinger equation using (2.8). For a polariton with quantum numbers (n, k), the state at time t is

$$|\psi(t)\rangle = e^{-i\omega_{nk}t} \times \left[-\phi_{nk}^1 \sigma_k^{ab} + \phi_{nk}^2 e^{i\omega_L t} \sigma_{k-k_L}^{cb} + \phi_{nk}^3 a_k^\dagger \right] |0\rangle. \tag{2.19}$$

The σ^{cb} component in (2.19) has a different frequency and wavevector compared to the rest of the polariton. This property does not, however, destabilize the polariton: in a wavepacket constructed of a superposition of dark-state polaritons, the photonic and σ^{cb} components possess different phase factors but share a single envelope.

The preceding derivation holds regardless of the angle between the input photon and the control beam. The direction of k_L only enters into the choice

of excitation operator $\sigma^{cb}_{k-k_L}$ occurring in the polariton operator (2.13), and plays no role in the eigenproblem (2.14) that yields the state amplitudes and polariton energy.

By switching between two non-collinear control beams, it is possible to coherently rotate the photon wavevector, by an angle of up to $2\sin^{-1}(\omega_{ac}/\omega_{ab})$, where the plane of rotation is specified by the polarization of the control field. A special case of this has been discussed by Juzeliūnas and Carmichael: when $\omega_b \approx \omega_c$, one can coherently backscatter the photon by inserting a photon with $k \sim k_L$, which mixes with a σ^{bc} excitation with wavevector $k - k_L \sim 0$, and switching the control field to $-k_L$. The σ^{bc} excitation then mixes into a photon of wavevector $k - 2k_L \sim -k$[27].

2.3   Double-Λ system

Suppose we add a second excited state, $|d\rangle$, as shown in Fig. 2.1(b). A second control beam couples $|d\rangle$ to $|c\rangle$, and for simplicity we assume that the two control beams have parallel polarization vectors. The $d \leftrightarrow a$ transition is assumed to be forbidden.

One of the reasons this "double-Λ" system is interesting is that it can be used to upconvert or downconvert probe beams, as experimentally demonstrated by Merriam *et. al.*[32] and other groups. It can be shown, using the Fleischhauer-Lukin formalism, that this type of level structure supports a dark-state polariton[30]. As we shall see, this dark-state polariton arises nat-

urally from the present method as a 5×5 generalizion of (2.14).

The Hamiltonian, $H'(t)$, contains several new terms. First, we have the Hamiltonian for the free $|d\rangle$ states, and the Hamiltonian for a second photon field with operators $b_k^\dagger$ and b_k:

$$\hbar \sum_r \left(\omega_d \sigma_r^{dd} \right) + \sum_k \hbar c |k| b_k^\dagger b_k. \tag{2.20}$$

There is really only one photon field, but introducing this second photon field is permissible since the atom-photon coupling becomes negligible far away from the EIT resonances.

We also have an additional set of interaction terms, which are analogous to (2.4) and (2.5):

$$-\hbar g' \sum_k b_k \sigma_k^{db} \hbar \Omega' - e^{-i\omega_L' t} \sum_r e^{ik_L' r} \sigma_r^{dc} + -\text{h.c.} \tag{2.21}$$

We now have two control field interaction Hamiltonians, associated with two different frequencies ω_L and ω_L'. Therefore, the transformation (2.6)-(2.7), which works by rotating $|c\rangle$, cannot eliminate the time dependence. We can overcome this difficulty with a transformation that instead rotates $|a\rangle$, $|d\rangle$, and the photon states. Let

$$H_L' = U_L'(t) H'(t) U_L'^\dagger$$
$$- \hbar \omega_L \left(\sum_k a_k^\dagger a_k + \sum_r \sigma_r^{aa} \right) - \hbar \omega_L' \left(\sum_k b_k^\dagger b_k + \sum_r \sigma_r^{dd} \right), \tag{2.22}$$

where $H'(t)$ is our new Hamiltonian, and

$$U'_L = \exp\left[i\omega_L t \left(\sum_k a_k^\dagger a_k + \sum_r \sigma_r^{aa} \right) + i\omega'_L t \left(\sum_k b_k^\dagger b_k + \sum_r \sigma_r^{dd} \right) \right].$$

(2.23)

This once again allows us to write the Schrödinger equation as

$$i\hbar \partial_t \left[U'_L(t) \left| \psi(t) \right\rangle \right] = H'_L \left[U'_L(t) \left| \psi(t) \right\rangle \right],$$

(2.24)

where H'_L is time-independent. We look for excitation operators

$$A_{nk}^\dagger = -\phi_{nk}^1 \sigma_{k+k_L}^{ab} - \phi_{nk}^2 \sigma_{k+k'_L}^{db} + \phi_{nk}^3 \sigma_k^{cb} + \phi_{nk}^4 a_{k+k_L}^\dagger + \phi_{nk}^5 b_{k+k'_L}^\dagger.$$

(2.25)

The self-consistency equations for the parameters ϕ_{nk}^j take the form

$$\mathcal{H}'_k \begin{bmatrix} \phi^1 \\ \vdots \\ \phi^5 \end{bmatrix}_{nk} = \omega_{nk} \begin{bmatrix} \phi^1 \\ \vdots \\ \phi^5 \end{bmatrix}_{nk},$$

(2.26)

$$\mathcal{H}'_k = \hbar \begin{bmatrix} \omega_{ab} - \omega_L & 0 & \Omega & g & 0 \\ 0 & \omega_{db} - \omega'_L & \Omega' & 0 & g' \\ \Omega^* & \Omega'^* & \omega_{cb} & 0 & 0 \\ g^* & 0 & 0 & c|k + k_L| - \omega_L & 0 \\ 0 & g'^* & 0 & 0 & c|k + k'_L| - \omega'_L \end{bmatrix}.$$

(2.27)

The polariton created by (2.25) is a valid excitation because, as in the single-Λ case, no extra non-negligible terms are generated by commutating this operator with the Hamiltonian.

Let us now assume that the control fields are resonant, i.e. $\omega_L = \omega_{ac}$ and $\omega'_L = \omega_{dc}$. For $|k+k_L| = \omega_{ab}/c$ and $|k+k'_L| = \omega_{db}/c$, the effective Hamiltonian (2.27) has an eigenvector

$$
\begin{bmatrix} \phi^1 \\ \vdots \\ \phi^5 \end{bmatrix}_{\text{DSP}} \propto \begin{bmatrix} 0 \\ 0 \\ 1 \\ -\Omega/g \\ -\Omega'/g' \end{bmatrix}. \tag{2.28}
$$

The first two components of this eigenvector, corresponding to the two excited states, are identically zero, so this represents a dark-state polariton consisting of σ_k^{cb} excitations and photons with wavevectors $k+k_L$ and $k+k'_L$. It can be shown that no other linearly independent eigenvector with this property exists, so there is only one such dark-state polariton solution. The linearized dark-state polariton solution, analogous to (2.16)-(2.18), is

$$
\omega_{nk} = \omega_{cb} + \frac{|\Omega/g|^2 \delta k + |\Omega'/g'|^2 \delta k'}{1 + |\Omega/g|^2 + |\Omega'/g'|^2} \tag{2.29}
$$

$$
\phi^1_{nk} = \frac{\Omega}{|g|^2} \frac{\delta k + |\Omega'/g'|^2(\delta k - \delta k')}{1 + |\Omega/g|^2 + |\Omega'/g'|^2} \phi^3_{nk} \tag{2.30}
$$

$$
\phi^2_{nk} = \frac{\Omega'}{|g'|^2} \frac{\delta k' + |\Omega/g|^2(\delta k' - \delta k)}{1 + |\Omega/g|^2 + |\Omega'/g'|^2} \phi^3_{nk} \tag{2.31}
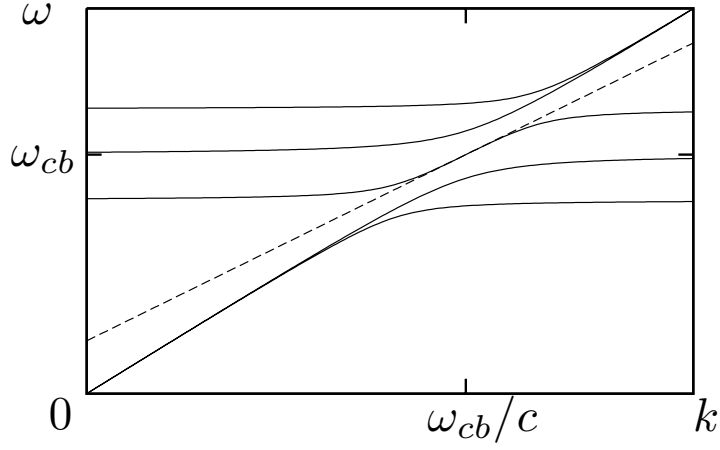$$

Figure 2.3: Polaritonic dispersion curve for the double-Λ medium. The solid lines show the exact polariton solutions given by Eq. (2.27); the dashed line shows the linearized solution given by Eq. (2.29). The horizontal asymptotes occur at ω_{cb} and $\omega_{cb} \pm \sqrt{|\Omega|^2 + |\Omega'|^2}$.

$$\phi^4_{nk} = -(\Omega/g)\,\phi^3_{nk} \tag{2.32}$$

$$\phi^5_{nk} = -(\Omega'/g')\,\phi^3_{nk}, \tag{2.33}$$

where $\delta k \equiv |k + k_L| - \omega_{ab}/c$ and $\delta k' = |k + k'_L| - \omega_{db}/c$. The polaritonic bandstructure, in the absence of loss, is shown in Fig. 2.3.

These results can be shown to be consistent with the single-photon limit of a semiclassical analysis of the double-Λ medium given by Korsunsky and Kosachiov[31]. In this one-dimensional model, where the electromagnetic field is treated classically, the Heisenberg equations of motion for the atomic system possesses a stationary "dark state" solution that is decoupled from the electromagnetic field and is stable against spontaneous emission. This dark state exists only if the background field (consisting of two probe beams and

two control beams) obeys certain frequency, amplitude, and phase matching

conditions. The frequency-matching condition is

$$\omega - \omega_L = \omega' - \omega'_L \;\; = \;\; \omega_{cb}, \tag{2.34}$$

where ω and ω' are the respective frequencies of the probe beams resonant

with the ab and db transitions. This equation is exactly satisfied by (2.25),

for which $\omega = c(k + k_L)$ and $\omega' = c(k + k'_L)$. The physical meaning of

(2.34) is particularly easy to deduce in the present theory: in the single-

photon limit, the stationary state corresponds to a polaritonic solution of

the form (2.25), for which the photonic components cannot take on arbitrary

frequencies because they are coherently mixed via the atomic excitation σ_k^{cb}.

The amplitude-matching condition for the semiclassical dark state is

$$\frac{\mathcal{P}E}{\Omega} = \frac{\mathcal{P}'E'}{\Omega'}, \tag{2.35}$$

where $\mathcal{P}$ and $\mathcal{P}'$ are the dipole moments for the ab and db transitions, and E

and E' are the electric field amplitudes of the associated probe beams. The

electric field amplitudes can be related to the quantum mechanical photon

amplitudes ϕ^4 and ϕ^5 by

$$E \;\; \leftrightarrow \;\; \sqrt{2\pi\hbar\omega_{ab}/V}\, \phi^4 \tag{2.36}$$

$$E' \;\; \leftrightarrow \;\; \sqrt{2\pi\hbar\omega_{db}/V}\, \phi^5, \tag{2.37}$$

which can be verified by computing the expectation value $\langle |E|^2 \rangle$ produced by each photon creation operator. With this identification, the linearized dark-state polariton amplitudes (2.32) and (2.33) satisfy (2.35). The third condition derived by Korsunsky and Kosachiov, which relates the phases of the four beams, is also satisfied by the dark-state polariton because, as shown by (2.32) and (2.33), the phases of the probe beams are locked to those of the control beams Ω and Ω'.

The dark state studied by Korsunsky and Kosachiov is a pure state of the atomic system, reflecting the fact that the electromagnetic field is treated classically[31]. In contrast, the present model takes into account the coherent mixing between the quantum state of the probe field and the quantum state of the atomic medium: performing a partial trace of the dark-state polariton over the photonic Hilbert space yields a mixed atomic state. This mixing becomes important at the single-photon level, which is also potentially the regime of interest for quantum information processing. In the following section, we will examine how this mixing can be used to convert between the two photonic components of the double-Λ dark-state polariton.

2.4 Frequency Conversion

For a single-Λ medium with a resonant control beam, inserting a photon with wavevector k_0, resonant with the ab transition, gives rise to a dark-state polariton whose group velocity points in the same direction, independent of

the direction of the control beam. This freedom to choose the direction of the control beam disappears in the double-Λ case. Here, an incident photon k_0 mixes with another photon with wavevector $k_1 = k_0 - k_L + k_L'$. Assuming both control beams are tuned to resonance, the resulting state overlaps with a dark-state polariton only if $|k_1| \simeq \omega_{db}/c$. Furthermore, the group velocity of the dark-state polariton is, from (2.29),

$$v = \nabla_k \omega_{nk} = \frac{|\Omega/g|^2\, \hat{k}_0 + |\Omega'/g'|^2\, \hat{k}_1}{1 + |\Omega/g|^2 + |\Omega'/g'|^2}, \qquad (2.38)$$

where $\hat{k}_0 = k_0/|k_0|$ and $\hat{k}_1 = k_1/|k_1|$. Therefore, a choice of $\hat{k}_0$ and $\hat{k}_1$ determines the directions of the two control beams (or, more generally, choosing any two of these directions determines the other two).

As an aside, we note that the beam matching conditions forbid the choice $\hat{k}_0 = -\hat{k}_1$, which would imply the possibility of a stationary wavepacket with nonzero control beams; however, if $\hat{k}_0$ and $\hat{k}_1$ are *nearly* antiparallel, (2.38) predicts that the control beam strengths can be tuned to produce a low group velocity.

In order to illustrate the mixing between the two photonic components in the dark-state polariton, let us fall back on the "trivial" one-dimensional case where all wavevectors are parallel, which satisfies the above beam matching conditions. Suppose we inject the photon k_0 at $t = 0$, so that the quantum state is

$$|\psi(0)\rangle = a_{k_0}^\dagger |0\rangle = \sum_{n=1}^{5} \phi_{nk}^{*\,4} A_{nk}^\dagger |0\rangle, \qquad (2.39)$$
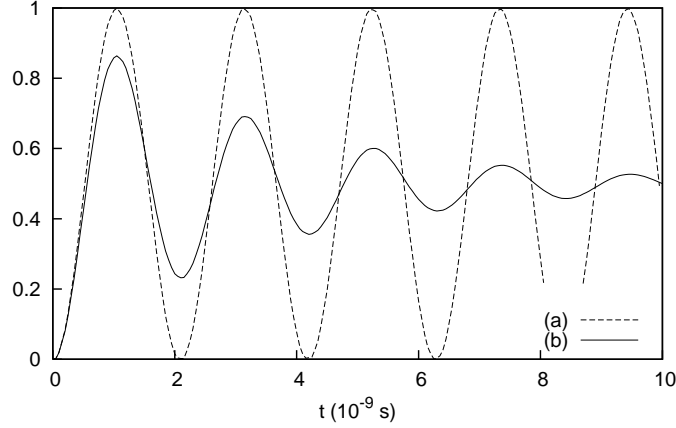
Figure 2.4: Numerical solutions of $|\langle 0| b_{k-k_L+k'_L} |\psi(t)\rangle|$ against t, where $|\psi(t)\rangle$ is the quantum state at time t after inserting a photon $a^\dagger_k$ with $k = \omega_{ab}/c$. Here, $\omega_{cb} = 10^4 \, \text{cm}^{-1}$, $|g| = |g'| = 0.1 \, \text{cm}^{-1}$, and $|\Omega| = |\Omega'| = 1 \, \text{cm}^{-1}$. (a) No excited state decay, $\Gamma_a = \Gamma_d = 0$. (b) $\Gamma_a = \Gamma_d = 0.02 \, \text{cm}^{-1}$.

where $k \equiv k_0 - k_L$. Without losses, the state at time t is

$$|\psi(t)\rangle = e^{i\omega'_L t} \left(e^{-i\mathcal{H}'_k t/\hbar} \right)_{5,4} b^\dagger_{k+k'_L} |0\rangle + \cdots , \tag{2.40}$$

where the matrix $\mathcal{H}$ is defined in (2.27) and the omitted terms are the other polariton components. The result, shown in Fig. 2.4, is an oscillating upconversion amplitude $|\langle 0| b_{k+k'_L} |\psi(t)\rangle|$ that can approach 100%. The effects of incoherent excited state decay, which can be modeled by replacing ω_a with $\omega_a - i\Gamma_a$ and ω_d with $\omega_a - i\Gamma_d$ in (2.27), are also shown in Fig. 2.4. Although the dark-state polaritons are protected against decay, damping still occurs because the incident photon generates a non-vanishing population of bright polaritons. When these exit the system (typically as off-axis photons), only the dark-state polariton remains.
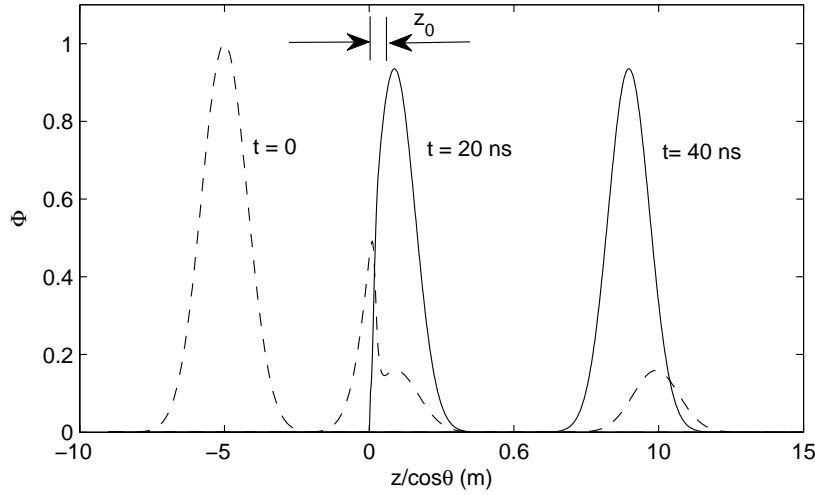
Figure 2.5: Photon frequency conversion. The *a*-photon amplitude $|\phi_4(z,t)|$ (dashed line) and *b*-photon amplitude $|\phi_5(z,t)|$ (solid line) are plotted at three instants. The abscissa is $z/\cos\theta$, where $k_L \cdot \hat{z} = \cos\theta$. The second control beam is pointed that $k'_L \cdot \hat{z} = 0.9\cos\theta$. Both control beams are c.w. The effective thickness of the double-Λ medium, $z_0 = 60\,\mathrm{cm}$, is indicated. Within the medium, $|g| = |g'| = 0.1\,\mathrm{cm}^{-1}$, $\Gamma_a = \Gamma_d = 0.2g$, $|\Omega| = 1\,\mathrm{cm}^{-1}$, and $|\Omega'| = 3\{1 + \tanh[4(z/\cos\theta - 0.5)/z_0]\}\,\mathrm{cm}^{-1}$. Outside the sample lies vacuum. The amplitudes are computed by integrating Eq. (2.42) numerically for the initial conditions in Eq. (2.44), where $\beta = 0.8\,\mathrm{m}^{-2}$ and $z_2 = -50\,\mathrm{cm}$.
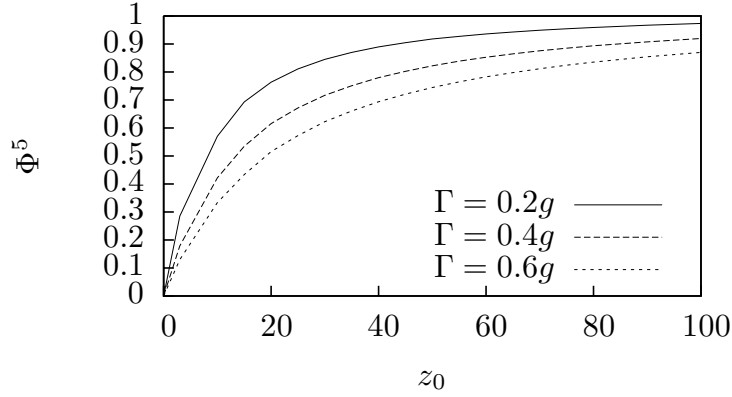
Figure 2.6: Frequency conversion efficiency, parameterized by the converted photon amplitude Φ^5 normalized to the input photon amplitude, as a function of the sample length z_0. Within the sample, the control beam Ω' varies as $|\Omega'| = 3\{1 + \tanh[4(z/\cos\theta - 0.5)/z_0]\}\,\mathrm{cm}^{-1}$. Curves for incoherent decay rates $\Gamma_a = \Gamma_d = 0.2g$, $0.4g$, and $0.6g$ are shown. All other parameters are the same as in Fig. 2.5.

A more efficient example of single-photon frequency conversion can be obtained by going from momentum space to real space and studying the behavior of polariton wavepackets. Let us define c-number fields $\Phi_j = \Phi_j(r,t)$ such that

$$|\psi(t)\rangle = \sum_r e^{i(\kappa r - \omega_{cb}t)}\left(-\Phi_1\,e^{ik_L r}\sigma_r^{ab} - \Phi_2\,e^{ik'_L r}\sigma_r^{db}\right.$$
$$\left. +\Phi_3\,\sigma_r^{cb} + \Phi_4\,e^{-ik_L r}a_r^\dagger + \Phi_5\,e^{-ik'_L r}b_r^\dagger\right). \quad (2.41)$$

Inserting (2.41) into the Schrödinger equation and using (2.27), we obtain a

Schrödinger *wave* equation

$$i\hbar \frac{\partial \Phi_i}{\partial t}(r, t) = \sum_j \mathcal{H}_{ij} \, \Phi_j(r, t). \tag{2.42}$$

If κ is chosen such that $|\kappa + k_L| = \omega_{ab}/c$ and $|\kappa + k'_L| = \omega_{db}/c$, then the dark-state polariton corresponds to values of Φ_j that are constant in space. For a wavepacket centered around κ with bandwidth $\ll \omega_{ab}$, ω_{db} (i.e., spatial width much longer than the optical wavelength, which is the usual slowly-varying envelope approximation), $\mathcal{H}$ takes on the intuitive local form

$$\mathcal{H}(r, t) \approx \hbar \begin{bmatrix} 0 & 0 & \Omega & g & 0 \\ 0 & 0 & \Omega' & 0 & g' \\ \Omega^* & \Omega'^* & 0 & 0 & 0 \\ g^* & 0 & 0 & -ic\hat{k}_0 \cdot \nabla & 0 \\ 0 & g'^* & 0 & 0 & -ic\hat{k}_1 \cdot \nabla \end{bmatrix}. \tag{2.43}$$

As in the single-Λ case, the evolution of the polaritonic envelope is independent of the underlying double-Λ frequencies, except through the coupling parameters g, g', Ω, and Ω'. We again emphasize that this result is not perturbative; it holds for arbitrary values of Ω and Ω', and depends only on the fact that the wavepacket is sufficiently broad. Generally, the coupling parameters can vary (smoothly) in space; for instance, a variation in Ω or Ω' could be accomplished using a c.w. control beam with a non-uniform cross-sectional intensity profile. Such variations can be used to "adiabatically"

transfer one photon population to another within a propagating dark-state polariton wavepacket, substantially improving the efficiency of the conversion process compared to the previous example.

Let us consider an effectively one-dimensional experimental setup where all relevant spatial variations occur in the z direction. In particular, we must assume that the x and y edges are far enough away that boundary effects (which appear when the beams are not all collinear) are negligible. The incident envelope field $\Phi_j(z, t = 0)$ is

$$\Phi_4 = \exp\left[-\beta\left(\frac{z}{\cos\theta} - z_2\right)^2\right],$$
$$\Phi_1 = \Phi_2 = \Phi_3 = \Phi_5 = 0.$$

(2.44)

Outside the sample ($z < 0$ or $z > z_0$), all coupling parameters are zero. Within the sample ($0 < z < z_0$), the functional forms of $\Omega(z)$ and $\Omega'(z)$ are chosen so that $|\Omega| > |g| > |\Omega'|$ near the entrance of the sample, which ensures that the dark-state polariton is dominated by the input photon; whereas $|\Omega'| > |\Omega| > |g|$ near the exit, which ensures that the dark-state polariton is dominated by the converted photon. The result is shown in Fig. 2.5. For the given parameters, the converted photon amplitude is ~ 0.9 times the incident amplitude. The efficiency is limited by the available length of the double-Λ medium. As shown in Fig. 2.6, a longer sample allows the Ω' field to be varied more gently, generating fewer bright state polaritons and increasing the conversion efficiency.

2.5 Conclusions

In this chapter, I have presented an analysis of single- and double-Λ EIT systems based on a microscopic equation-of-motion technique. Within this formalism, the presence of a dark-state polariton corresponds to the existence of special eigenvectors of an effective Hamiltonian matrix, in which the entries corresponding to rapidly decaying excitations are identically zero, regardless of the strength of the control fields. The ability of the double-Λ system to efficiently upconvert and downconvert photons, previously established in semiclassical four-wave mixing studies[31,32], is retained in the coherent single-photon limit due to the existence of the dark-state polariton. The analysis can be further generalized to multi-Λ systems, where one finds additional polaritonic bands similar to those in Fig. 2.3, with exactly one family of dark-state polariton solutions possessing vanishing excited state populations.

This theory is concerned with only the single-polariton sector, which is valid only if the polaritons are much more dilute than the underlying atomic medium. The polariton operators (2.13) and (2.39) do not obey exact bosonic commutation relations, since the σ operators are not bosonic operators; however, the corrections to the commutator vanish as $O(M/N)$, where M is the number of atoms excited[20]. This condition is satisfied, for instance, in the experiments of Merriam *et. al.*, where $M/N \sim 10^{-3}$[32]. The single-polariton sector has the advantage that the quantum state of the system can be expressed in terms of a simple wave equation, as in (2.42). Thus, once the σ

operators have been used to derive the effective Hamiltonian, the additional structure given by their non-trivial commuation relations disappears from the theory. Should one wish to study the limit where M becomes comparable to N, this structure will have to be taken into account.

We now turn away from the topic of atomic-lattice photonic crystals. Chapters 3 and 4 deal with a class of photonic crystals that deviate from the conventional photonic crystal theory in a completely different way. These are solid-state photonic crystals in which time-reversal symmetry is broken. As we shall see, the systems exhibit some truly remarkable properties, including interface modes that are immune to backscattering.

Chapter 3

One-way Edge Modes in Magneto-optic Photonic Crystals

3.1 Non-reciprocal photonic crystals

Let us recall how time-reversal symmetry applies to Maxwell's equations. Suppose the electromagnetic fields and sources vary harmonically with frequency ω, so that we can adopt the usual complex representation: if the real electric field is $\vec{\mathcal{E}}(t)$, the corresponding complex electric field E is defined by

$$\vec{\mathcal{E}}(t) = \mathrm{Re}\left[Ee^{-i\omega t}\right]. \tag{3.1}$$

---

*Z. Wang, Y. D. Chong, J. D. Joannopoulos, and M. Soljačić, Phys. Rev. Lett. **100**, 013905 (2008).

Complex representations for the other fields and sources are defined similarly. The linear Maxwell equations then become

$$\nabla \cdot \vec{D} = \rho_f, \qquad \nabla \cdot \vec{B} = 0,$$
$$\nabla \times \vec{E} = i\omega \vec{B}, \qquad \nabla \times \vec{H} = J - i\omega \vec{D}, \tag{3.2}$$

where

$$\vec{D} = \epsilon \vec{E} \qquad \text{and} \qquad \vec{H} = \mu^{-1} \vec{B}. \tag{3.3}$$

The system is said to obey time-reversal symmetry if, for each solution

$$\left\{ \vec{E}, \vec{D}, \vec{B}, \vec{H}, \rho, \vec{J} \right\}, \tag{3.4}$$

the following is also a solution to (3.2) and (3.3):

$$\left\{ \vec{E}^*, \vec{D}^*, -\vec{B}^*, -\vec{H}^*, \rho^*, -\vec{J}^* \right\}. \tag{3.5}$$

This is called a "time-reversed" solution because of the way we have defined the complex fields and sources. For example, returning to (3.1):

$$\vec{\mathcal{E}}(-t) = \mathrm{Re}\left[E e^{i\omega t} \right] = \mathrm{Re}\left[E^* e^{-i\omega t} \right]. \tag{3.6}$$

It is a quirk of Maxwell's equations that time-reversal requires flipping the signs of the magnetic field and current density, as indicated in (3.5); we will simply take this as our operational definition of time-reversal symmetry for

electromagnetic systems. By direct substitution, we then see that (3.5) is a valid solution to (3.2). It is also a valid solution to (3.3) *if and only if ϵ and μ are real*. This is normally the case (e.g. in the simplest case where ϵ and μ are real scalars), but not always. If non-radiative losses are absent, ϵ and μ are Hermitian tensors, and time-reversal symmetry may be broken by introducing non-zero imaginary terms to the off-diagonal components of one or both of these tensors.

We should note, at this point, that it is easy to break time-reversal symmetry, by (i) introducing non-radiative losses or (ii) adding non-harmonic time-dependences to ϵ or μ. For the moment, let us ignore these "trivial" sources of time-reversal symmetry breaking.

The materials that we are interested in are those in which ϵ and/or μ contain imaginary off-diagonal components. These are called "non-reciprocal media", as their electromagnetic properties are dependent on the direction of time. More prosaically, we could say that they respond differently to an applied electromagnetic field and its time-reversed counterpart. They are also referred to as "magneto-optical media" because, as we will see, the non-reciprocity typically arises when the microscopic currents within the medium are "pinned" by an external magnetic field. These materials are commonly used in Faraday isolators, devices that allow the transmission of electromagnetic waves moving in one direction while absorbing waves of equal frequency moving in the opposite direction.

Several authors have investigated the use of non-reciprocal media in pho-

tonic crystals[37,38]. For example, it has been shown that one-dimensional photonic crystals made of non-reciprocal media can give rise to an enhanced Faraday rotation angle (i.e., the angle by which the polarization vector of a plane wave rotates as it passes through the system). However, the most remarkable phenomenon associated with such photonic crystals was pointed out only recently, by Haldane and Raghu[16,17]. These authors predicted that certain two-dimensional non-reciprocal photonic crystals possess electromagnetic edge modes that are analogous to electronic edge states in the integer quantum Hall effect[18]. These modes are remarkable because they possess group velocities pointing in only one direction along the edge, regardless of detailed shape of the edge. The direction is determined by the sign of the time-reversal symmetry breaking within the bulk crystal, and the time-reversed versions, which propagate in the reverse direction, are not valid eigenmodes.

If electromagnetic one-way modes could be realized, suitable applications would readily be found. For example, it has long been known that photonic crystals can be used to construct slow-light waveguides. However, such structures are extremely susceptible to backscattering, which limits their efficiency[39]. A slow-light waveguide utilizing one-way modes could overcome this limitation as the the backscattered modes would be evanescent.

In this chapter, I will discuss how the one-way edge modes predicted by Haldane and Raghu can be practically realized. I will begin by reviewing the necessary conditions for the existence of these modes, which are related

to the topological properties of the photonic bandstructure. Based on these
conditions, Haldane and Raghu have suggested using triangular-lattice pho-
tonic crystals incorporating gyroelectric materials. Though valid in principle,
this proposal turns out to run into serious practical difficulties. I will present
an experimentally feasible photonic crystal incorporating gyromagnetic ma-
terials, which should allow one-way edge modes to be easily observed. This
photonic crystal possesses a bandstructure with the desired non-trivial topol-
ogy, but deviates from the Haldane-Raghu theory in some interesting ways.
I will present numerical simulations that demonstrate the existence of the
edge modes and their immunity to backscattering. In the next chapter, I will
develop an analytical theory for the bandstructure of this photonic crystal.

3.2   Topological effects

The existence of one-way edge modes in photonic crystals is related to the
concept of the Chern number, an integer quantity associated with each band
in a two-dimensional Bloch system[40–42]. The Chern number measures a cer-
tain topological property of the band. A self-contained introduction to this
topic is provided in Appendix A.

   Although the Chern number was first introduced to physics in the con-
text of electronic bands in the quantum Hall effect, Haldane and Raghu[16,17]
have pointed out that the concept is not limited to electronic systems. The
Chern number can be defined in any two-dimensional Hermitian system

with discrete translational symmetry (i.e. any Bloch system), including two-dimensional photonic crystals. In the absence of free charges and currents, Maxwell's equations can be cast as a Hermitian eigenproblem[2]. There are several ways to accomplish this; we will pick one that is useful for our purposes.

Let us assume that μ is a Hermitian tensor, while ϵ is a scalar. (It is possible to analyze the more general case where both ϵ and μ are tensors, but this is significantly more complicated[16,17]. Furthermore, it is not relevant for the materials that we will consider.) We eliminate the magnetic field from Maxwell's equations to express them in terms of the electric field $\vec{E}(r)$. (The conventional band theory of photonic crystals[2] eliminates $\vec{E}$ to express things in terms of $\vec{H}$; we shall see why the present choice makes sense for us.) For a mode with frequency ω,

$$\epsilon^{-1}(r)\, \nabla \times \left(\boldsymbol{\mu}^{-1}(r)\nabla \times \vec{E}(r)\right) = \omega^2 \vec{E}(r). \tag{3.7}$$

Here, both the inverse permeability tensor $\boldsymbol{\mu}^{-1}$ and the scalar ϵ are functions of position. Let us define the inner product as

$$\langle E_1|E_2\rangle = \int d^2r \ \epsilon(r)\vec{E}_1^* \cdot \vec{E}_2, \tag{3.8}$$

where $|E\rangle$ represents the eigenket (abstract state vector) associated with the eigenmode whose field is $\vec{E}(r)$. Using this inner product, it is easily shown that the operator on the left hand side of (3.7) is a Hermitian operator.

If ϵ and μ are periodic, (3.7) further reduces to a Bloch problem, and the eigenkets can be written in the Bloch form $|nk\rangle$. Let us define the quantity

$$\vec{\mathcal{A}}^{nn'}(k) \equiv \langle nk|\nabla_k|n'k\rangle \,, \tag{3.9}$$

called the "Berry connection", where the inner product for Bloch states is identical to (3.8) except that the integral is performed over a single unit cell.

For each band n, the Chern number is

$$C_n = \frac{1}{2\pi i} \int_{BZ} d^2k \left(\frac{\partial \mathcal{A}_y^{nn}}{\partial k_x} - \frac{\partial \mathcal{A}_x^{nn}}{\partial k_y} \right) \,, \tag{3.10}$$

where the k-space area integral is performed over the first Brillouin zone. As shown in Appendix A, the Chern number has the following properties:

1. It is always an integer.

2. The sum of the Chern numbers over all bands is zero.

3. The Chern number of every band is zero if the Hamiltonian is symmetric under time-reversal or parity.

These properties imply that as one adiabatically tunes the Hamiltonian (e.g., varying the strength of the permeability tensor), the Chern number of each band changes, if and when it does so, abruptly. The critical point at which this abrupt change occurs is exactly when the band becomes degenerate with a neighboring band at one or more k-space points.

If the system is tuned correctly, the band's Chern number changes by a non-zero integer p once the degeneracy is lifted. At the same time, the other band's Chern number changes by $-p$. This tuning must involve time-reversal symmetry breaking, since all Chern numbers are zero when the system is time-reversible. Hatsugai[43] has shown that in a lattice quantum Hall model, this gives rise to p one-way edge states that occupy the gap between the two bands. As far as I know, no equivalent theorem has been proven for photonic crystals. However, there is an interesting relationship that allows us to map photonic modes to a family of QH systems. Suppose, as before, that the permittivity is a scalar and the permeability a Hermitian tensor. We write the inverse permeability tensor as

$$\boldsymbol{\mu}^{-1} = \begin{bmatrix} \nu^{-1} & i\eta & 0 \\ -i\eta & \nu^{-1} & 0 \\ 0 & 0 & \mu_0^{-1} \end{bmatrix}. \tag{3.11}$$

Plugging this into (3.7), we find that the equations for E_x and E_y decouple from E_z. For TM states ($E_x = E_y = 0$),

$$\left[-\nabla^2 + (\nabla \ln \nu - i\nu \hat{z} \times \nabla \eta) \cdot \nabla - \nu \epsilon \omega^2 \right] E_z = 0. \tag{3.12}$$

Expressing this in terms of $\psi \equiv E_z/\sqrt{\nu}$, we obtain

$$\left[-\left| \nabla + i\tilde{A}(r) \right|^2 + \tilde{V}(r) \right] \psi = 0, \tag{3.13}$$

where

$$\tilde{A} = \frac{\nu}{2}\,\hat{z} \times \nabla\eta, \tag{3.14}$$

$$\tilde{V} = \frac{1}{4}\left(|\nabla \ln \nu|^2 + |\nu\nabla\eta|^2\right) - \frac{1}{2}\nabla^2 \ln \nu - \nu\epsilon\omega^2. \tag{3.15}$$

This is the equation for zero-energy wavefunctions of a non-relativistic particle in periodic vector and scalar potentials $\tilde{A}(r)$ and $\tilde{V}(r)$. Increasing ω corresponds to increasing the depth of the scalar potential well in the third term of (3.15), shifting the spectrum downwards relative to the zero of energy. With suitable boundary conditions, this mapping holds for both edge modes and bulk modes. Thus, for each value of ω, the existence of unpaired edge modes, as well as their spatial characteristics, can be mapped to a similar problem in a QH system.

Therefore, it appears that Hatsugai's result should be generally true; the only necessary condition is that there are no bulk modes beyond the boundary of the system. In the quantum Hall system, this is accomplished using an electrostatic potential well; in a photonic crystal, this can be accomplished by surrounding the crystal with a perfect electric conductor, or with a second photonic crystal possessing a complete bandgap at the operating frequency. In theory, the one-way edge modes appear as soon as the degeneracy is lifted, but in practice they are physically relevant only if the lateral confinement to the edge is fairly tight. The confinement is roughly $\omega/\Delta\omega$ lattice constants, where $\Delta\omega$ is the size of the bandgap. If this is too large, the bandgap will
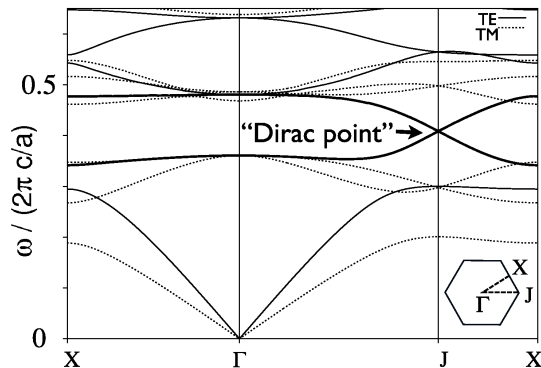
Figure 3.1: Bandstructure of a hexagonal lattice of dielectric rods, with filling fraction 0.431 and $\epsilon = 14$. A linear degeneracy, or "Dirac point", occurs between the second and third TE bands at each of the two equivalent corners of the hexagonal Brillouin zone. From Raghu and Haldane (2006)[17].

not be robust against disorder, and the edge modes will scatter easily into the bulk modes of the crystal, leading to significant radiative loss.

The above discussion implies a simple and general strategy for constructing photonic crystals supporting one-way edge modes. We begin by searching for a time-reversible band structure with a pair of photonic bands degenerate at one or more discrete k-points. If this degeneracy is broken when we alter the system in a manner that breaks time-reversal symmetry, it might be possbile to observe one-way edge modes within the resulting bandgap.

Haldane and Raghu identified hexagonal-lattice photonic crystals as a candidate system for observing one-way modes[16,17]. In a time-reversible photonic crystal consisting of dielectric rods in a hexagonal lattice, the second and third TE bands are degenerate at each of the two inequivalent corners of

the hexagonal Brillouin zone[44], as shown in Fig. 3.1. The bands meet linearly at these degeneracies, which are referred to as "Dirac points" because the Bloch modes in the vicinity of these degeneracies can be described in terms of an effective Dirac theory. Such theories have been extensively deployed in the condensed-matter literature. For instance, Dirac points arise in a famous model of a quantum Hall system, proposed by Haldane in 1988, consisting of tight-binding electron orbitals in a hexagonal lattice[45]. The Dirac theory predicts that the bands acquire Chern numbers of ± 1 when time-reversal symmetry is broken, which in turn implies the existence of one family of one-way edge modes.

In TE modes, the electric field vector lies parallel to the plane and the magnetic field lies perpendicular to the plane. Therefore, the only way for a time-reversal symmetry breaking effect to lift the TE band degeneracies is by introducing off-diagonal components to the permittivity tensor. Non-reciprocal materials with this property are called gyroelectric materials. Haldane and Raghu showed that the indicated degeneracies can be lifted by adding a gyroelectric effect to the medium outside the rods, and that this gives rise to the predicted one-way edge modes.

The main problem with the Haldane-Raghu proposal is that real gyroelectric materials break time-reversal symmetry very weakly. The ratio of (imaginary) off-diagonal to (real) on-diagonal elements of the permittivity tensor (the Voigt parameter) is $\sim 10^{-3}$ for the best materials available. This is also roughly the ratio of the bandgap to the operating frequency, which,

as we have discussed, implies that the edge modes span thousands of lattice spacings and are readily scattered into the bulk. In order to actually observe this effect, one would desire a bandgap that is orders of magnitude larger.

3.3 Photonic crystal bandstructure

In this section, I will describe a type of photonic crystal that supports one-way edge modes without the restriction of having Dirac points in the bandstructure or the use of gyroelectric materials. With realistic material parameters, the one-way edge modes are laterally confined to a few lattice constants, and occupy a broad ($\sim 10\%$) band-gap with negligible material loss. The system consists of Yttrium-Iron-Garnet (YIG) elements in a square lattice, which lacks Dirac points in its bandstructure, operating at microwave frequencies.

The YIG elements in the photonic crystal are gyromagnetic ferrimagnets[46]. These exhibit strong time-reversal symmetry breaking due to the phenomenon of ferromagnetic resonance. In the presence of an applied magnetic field $\vec{B}$, the local magnetic moment $\vec{M}$ obeys the precessional equation

$$\frac{d\vec{M}}{dt} = \gamma \vec{M} \times \vec{B}, \tag{3.16}$$

where γ is the gyromagnetic ratio. If $\vec{B}$ consists of a strong static out-of-plane

field plus in-plane components that are weaker and harmonic in time,

$$\vec{B} = [\delta B_x e^{-i\omega t}, \delta B_x e^{-i\omega t}, B_z], \tag{3.17}$$

then the magnetic moment has a similar form:

$$\vec{M} = [\delta M_x e^{-i\omega t}, \delta M_x e^{-i\omega t}, M_z]. \tag{3.18}$$

Here, $M_z = (\alpha_s/\mu_0)B_z$, where $\alpha_s = \chi_s/(1 + \chi_s)$, with χ_s denoting the static magnetic susceptibility. From (3.16), we obtain

$$\begin{bmatrix} \delta M_x \\ \delta M_y \end{bmatrix} = \frac{\alpha_s}{\mu_0} \frac{\omega_0}{\omega_o^2 - \omega^2} \begin{bmatrix} \omega_0 & i\omega \\ -i\omega & \omega_0 \end{bmatrix} \begin{bmatrix} \delta B_x \\ \delta B_y \end{bmatrix}, \tag{3.19}$$

where $\omega_0 = \gamma B_z$ is the magnetic resonance frequency. Therefore, the in-plane permeability tensor is

$$\mu_{\text{2D}} = \mu_o \left(1 - \frac{\alpha_s \omega_0}{\omega_o^2 - \omega^2} \begin{bmatrix} \omega_0 & i\omega \\ -i\omega & \omega_0 \end{bmatrix} \right)^{-1}. \tag{3.20}$$

This possesses an imaginary off-diagonal component because the presence of the static magnetic field B_z breaks time-reversal symmetry: if we reverse the direction of this field, the magnetic moments precess in the opposite direction, and the imaginary off-diagonal components switch sign. When $\omega \approx \omega_0$, the second term in (3.20) dominates the permeability, so time-reversal symmetry

can be strongly broken.

For simplicity, let us assume that the system is always operating in the vicinity of a reference frequency ω_1, where ω_1 is close to ω_0. We approximate the permeability tensor with the frequency-independent form

$$\boldsymbol{\mu}_{2\mathrm{D}} = \begin{bmatrix} \mu & i\kappa \\ -i\kappa & \mu \end{bmatrix},$$

(3.21)

obtained by evaluating (3.20) at $\omega = \omega_1$. For $\omega_1 = 26.9$ GHz ($f = \omega/2\pi = 4.28$ GHz), the tensor elements for YIG in a 1600 Gauss applied field are $\mu = 14\mu_0$ and $\kappa = 12.4\mu_0$[46]. (Later, we will examine the consequences of including the full ω-dependence, as well as material losses. It turns out that these effects are relatively unimportant.)

The breaking of time-reversal symmetry in the in-plane permeability tensor affects the TM modes, which contain in-plane magnetic fields and out-of-plane electric fields. Fig. 3.2 shows the TM bandstructure for a photonic crystal of YIG rods in a square lattice, surrounded by air. The bandstructure is computed numerically, using the COMSOL program[47]. Each rod has radius $0.11a$ (where a is the lattice constant) and permittivity $15\epsilon_0$. When no static out-of-plane magnetic field is applied, the permeability is μ_0, and the second and third TM bands are degenerate at the corner of the Brillouin zone (M). There is a separate degeneracy between the third and fourth TM bands at the center of the Brillouin zone (M). Unlike the degeneracies in the crystal studied by Haldane and Raghu, these degeneracies are quadratic
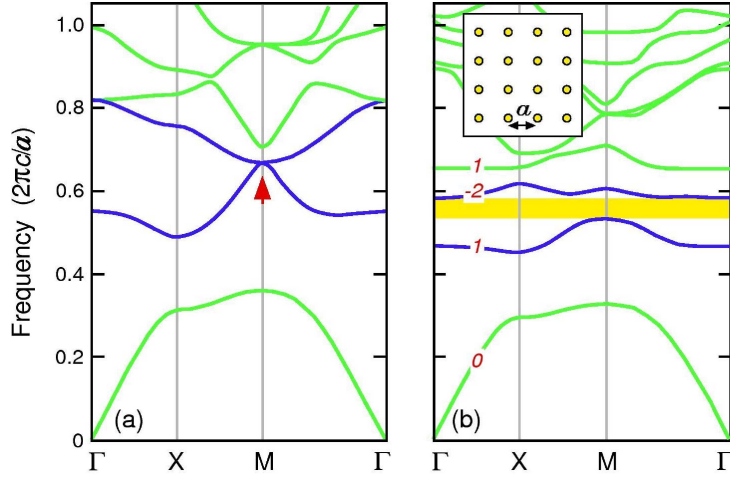
Figure 3.2: TM photonic bandstructure for a square lattice of YIG rods (inset in b, with and $r = 0.11a$) in air. (a) Zero static magnetic field. The relevant quadratic degeneracy point is indicated. (b) 1600 Gauss $+z$ static magnetic field. The degeneracies are lifted, resulting in non-zero Chern numbers (red numbers). The Chern numbers are calculated from Eq. 3.9.

and not linear "Dirac points". As we will see in the next chapter, linear degeneracies are forbidden by the C_{4v} symmetry of the square-lattice photonic crystal.

With a static 1600 Gauss out-of-plane magnetic field, the rods' permeability components (3.21) are $\mu = 14\mu_0$ and $\kappa = 12.4\mu_0$. The degeneracies are lifted, and a numerical calculation of the Chern numbers yields 1, -2, and 1 repectively. In other words, each degeneracy-lifting causes a Chern number exchange of magnitude $p = 1$. The bandgap between the second and third TM bands is around 10% of the operating frequency, which should be suitable for observing the one-way edge modes. We ignore the bandgap between the third and fourth bands, which is significantly smaller.

3.4   One-way edge modes

When the magnetized photonic crystal intersects a cladding in which the fields go to zero, one-way edge modes exist at the interface. The interface therefore functions as a one-way waveguide. Fig. 3.3 shows a simulation in which the cladding is an ordinary photonic crystal possessing a bandgap at the operating frequency. The cladding crystal consists of a square lattice of high-index alumina rods ($r = 0.106a, \epsilon = 10\epsilon_0$) in air, tilted 45 degrees to match the bandgap frequency. (The cladding crystal is time-reversible, and does not itself produce one-way edge modes.) The precise details of the interface does not really matter; for example, the one-way edge modes can also be observed along a boundary with a perfect electrical conductor. An antenna, inserted at the boundary and operating at a mid-gap frequency, excites a mode that propagates rightwards along the boundary. To the left of the antenna, the fields decay exponentially to zero.

The projected bandstructure of the system was computed in COMSOL[47], and the results are shown in Fig. 3.4. As we can see, a branch of unpaired edge modes occupies the gap between the second and third bulk TM bands. The fact that there is exactly one branch of edge modes is consistent with the discussion in the previous section, where we found that the degeneracy lifting induces a $p = 1$ Chern number transfer (Fig. 3.2). Another branch of one-way modes exists in the gap between the third and fourth TM bands, but it is not plotted in Fig. 3.4.
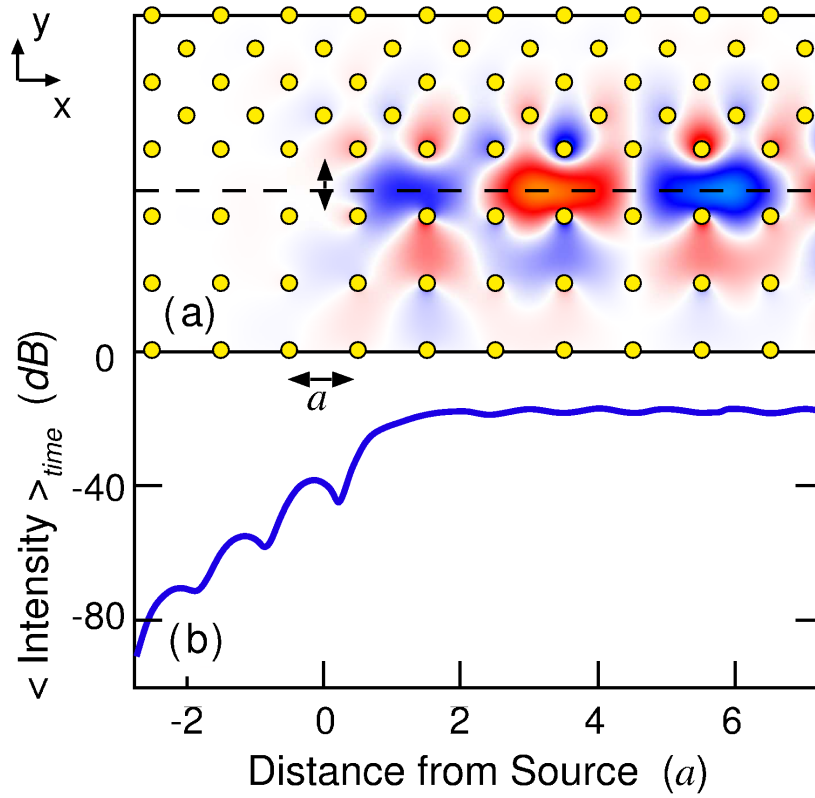
Figure 3.3: (a) Steady-state field pattern of a one-way edge mode at the interface between the magnetized YIG photonic crystal (lower half-plane) and a stopband cladding (upper half-plane). The field plotted is E_z, the out-of-plane electric field component, with blue and red representing positive and negative values respectively. The edge mode is excited by a c.w. source (black double-arrow) along the interface (dashed line), which operates at a mid-gap frequency $(0.552 \cdot 2\pi c/a)$. (b) Time-averaged value of $|E_z|^2$ along the interface.
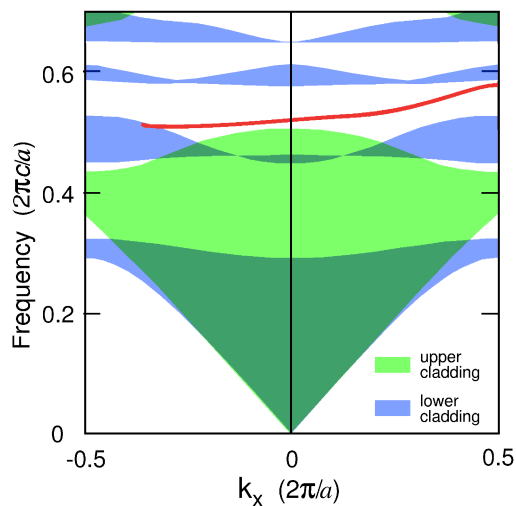
Figure 3.4: Projected band diagram at the boundary between the magnetized YIG photonic crystal and a stopband cladding. The bulk modes of the YIG crystal are shown in blue, those of the cladding are shown in green, and the dispersion curve of the edge modes is shown in red.

Numerical simulations show that the one-way edge modes are immune to scattering from extremely large defects inserted along the interface. Fig. 3.5 shows the results of simulations with a slab of perfect electrical conductor (PEC) of width $3a$ and thickness $0.2a$ placed perpendicular to the interface. In a conventional waveguide, such a drastic defect would almost completely block the guided mode. In the current system, a steady-state source operating at the mid-gap frequency $0.555 \cdot (2\pi c/a)$ excites a one-way mode that circumvents the PEC defect, with 100% power transmission within the bulk bandgap. This happens because the defect creates a new interface waveguide between the PEC and the magnetized crystal. It therefore only alters the phase response, which is partly due to the delay incurred by traversing the

lengthened interface.

The robustness of the one-way modes can be further quantified using a time-domain transmission calculation. Fig. 3.6 shows the electric field intensity along the interface after a temporal Gaussian pulse with a spectral bandwidth of 50% of the bandgap and carrier frequency $0.555 \cdot (2\pi c/a)$ is launched into the waveguide. Regardless of the presence of the defect, the pulse passes through the waveguide with no perceivable change in amplitude or pulse width. Since the one-way mode has approximately linear dispersion relation at mid-gap frequencies (Fig. 3.4), sharp corners do not contribute significantly to chromatic dispersion. The increased transit time is in agreement with the change in group delay.

Although embedded sources were used in the above simulations, a separate set of simulations have verified that it is also easy to couple to the one-way mode using waves incident on the system boundary.

3.5   Propects for experimental realization

Thus far, our analysis has been limited to two-dimensional structures. Similar one-way waveguides can be realized in practical three-dimensional structures. In the three-dimensional structure, TM modes can be truncated by sandwiching the rods of the photonic crystal between two slabs of perfect electrical conductor[46,48]. At microwave frequencies, metals such as copper can be treated as perfect electrical conductors. Since the electric field must be normal at the
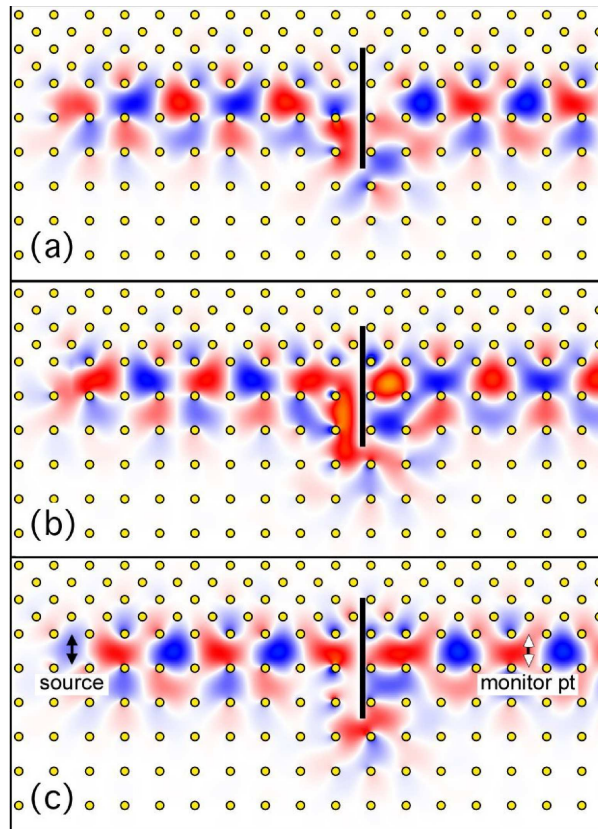
Figure 3.5: Back-scattering suppression in the one-way waveguide. When a slab of perfect electrical conductor with thickness $0.2a$ (black rectangle) is inserted, the propagating modes circumvent the defect and maintain complete transmission. The left hand side plots E_z for (a) $t = 0$, (b) $t = 0.25T_0$, and (c) $t = 0.5T_0$, where T_0 is the optical period.
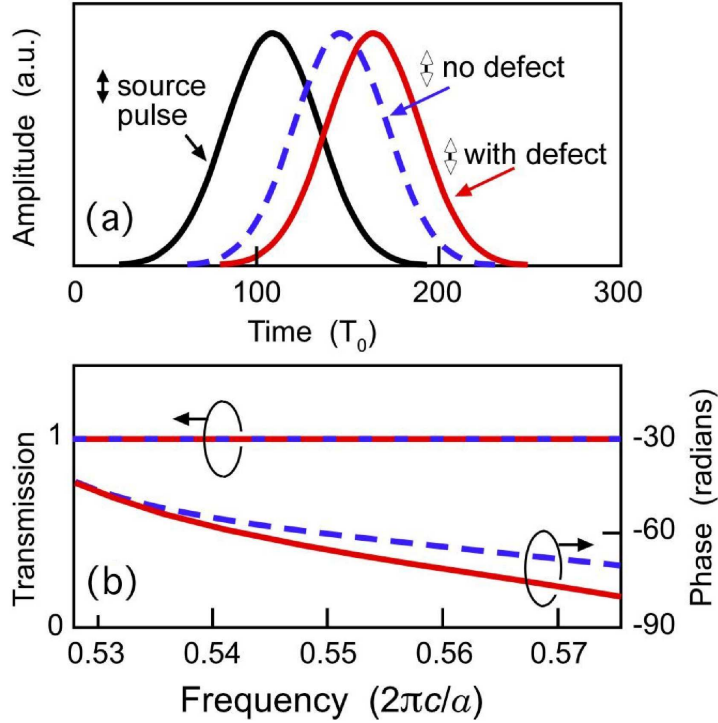
Figure 3.6: (a) Time-domain simulation results for a temporal Gaussian pulse with spectrum contained in the bandgap. The electric field amplitude is plotted at the source point (black), at the same transverse position 13 lattice constants downstream along the waveguide in the absence of a defect (red), and at the same point with an intervening defect (blue). (e) Transmission and phase shift plots for the time-domain simulation, showing that the pulse is completely transmitted regardless of the existence of the defect.

Figure 3.7: Photonic bandstructure for the second and third TM bands, with and without frequency dependence in the gyromagnetic permeability tensor.

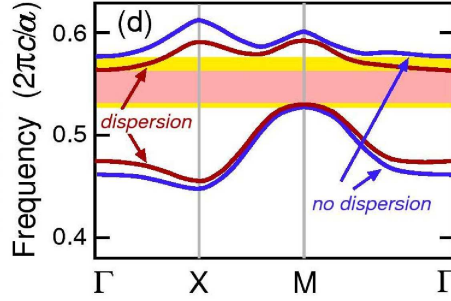surface of the conducting slabs, the three-dimensional structure supports the same field distributions as the two-dimensional system (assuming, of course, that the spacing between the slabs is sufficiently narrow that higher-order modes are not generated for the desired operating frequency). It should be noted that TE modes, like those studied by Haldane and Raghu[16,17], lack this advantage.

Real microwave ferrites contain material losses, which the simulations in the preceding section have ignored. Material losses will cause the one-way edge modes to decay, but for practical purposes this decay is quite negligible. With a gyromagnetic linewidth of 0.3 Oe and a dieletric loss tangent of 0.0002, typical in commerically available monocrystalline YIG[49], the complex propagation constant was found to be is $(-0.359+0.0001i)(2\pi/a)$ for the one-way edge mode shown in Fig. 3.5. This means that the decay length is around 300 lattice constants, far exceeding practical structural dimensions.

We have also ignored the frequency dependency of the gyromagnetic per-

meability, which was given in (3.20). Including the full frequency dependence modifies the photonic bandstructure slightly, as shown in Fig. 3.7. The magnetic bandgap shrinks from around 10% to around 6%, which narrows the operational bandwidth, though not fatally. Further simulations have shown that the dispersion does not harm the back-scattering suppression or the confinement of the edge mode.

Finally, it should be noted that the system we have studied is limited to the GHz regime. According to (3.20), the operating frequency of the gyromagnetic photonic crystal must lie near the magnetic resonance frequency. This can go up to several GHz in the presence of high-field biasing magnets, but no higher. In the GHz regime, the system is essentially a table-top experiment, which should make it relatively easy to create; as of this writing, an experimental effort is already underway. For applications at THz and higher frequencies, the prospects for realizing one-way edge modes remain uncertain. One possible avenue of attack is to invent a meta-material that produces an artificial high-frequency magnetic resonance. To the best of my knowledge, no suitable proposal currently exists in the literature.

Chapter 4

Effective theory of quadratic degeneracies

4.1 Quadratic degeneracies

In the previous chapter, we studied the bandstructure of a two-dimensional crystal with a square-lattice (C_{4v}) symmetry. This bandstructure contained band degeneracies at particular points in k-space: the center of the Brillouin zone (Γ) and the corner of the Brillouin zone (Γ). As we have seen, such degeneracies play an important role in the study of one-way edge modes: when the degeneracies are lifted by breaking time-reversal symmetry, the edge modes are generated within the resulting bandgap.

In the condensed-matter literature, a common approach to studying band

---

degeneracies is to construct an "effective theory", which characterizes the bandstructure near each degeneracy in a manner that is independent of the underlying physical details. Suppose we have a band degeneracy at $\vec{k} = \vec{k}_0$. Let us choose a pair of independent Bloch functions at $\vec{k}_0$, denoted by $u_0^1(\vec{r})$ and $u_0^2(\vec{r})$. Since we interested in $\vec{k} \sim \vec{k}_0$, let us define $\vec{\kappa} \equiv \vec{k} - \vec{k}_0$ for convenience. For $\vec{\kappa} \approx 0$, the Bloch functions can be written as

$$
\begin{aligned}
u_\kappa^1(\vec{r}) &\approx c_{11}(\vec{\kappa}) u_0^1(\vec{r}) + c_{12}(\vec{\kappa}) u_0^2(\vec{r}) \\
u_\kappa^2(\vec{r}) &\approx c_{21}(\vec{\kappa}) u_0^1(\vec{r}) + c_{22}(\vec{\kappa}) u_0^2(\vec{r}).
\end{aligned}
\tag{4.1}
$$

The mixing elements $c_{nm}(\vec{\kappa})$ can be related to the mode frequencies, $\omega_n(\vec{\kappa})$, through an eigenvalue equation

$$
H(\vec{\kappa})
\begin{bmatrix}
c_{n1}(\vec{\kappa}) \\
c_{n2}(\vec{\kappa})
\end{bmatrix}
= \lambda_n(\vec{\kappa})
\begin{bmatrix}
c_{n1}(\vec{\kappa}) \\
c_{n2}(\vec{\kappa})
\end{bmatrix},
\tag{4.2}
$$

where the "effective Hamiltonian" $H(\vec{\kappa})$ is a 2×2 matrix whose eigenvalues are, by definition, $\lambda_n(\vec{\kappa}) \equiv \omega_n(\vec{\kappa}) - \omega_0$. As we shall see, obtaining $H(\vec{\kappa})$ alone can provide a great deal of insight into the physical properties of the system, in a way that does not require any additional information about $u_0^1(\vec{r})$ and $u_0^2(\vec{r})$ (which are generally rather complicated functions of $\vec{r}$).

The seminal Haldane-Raghu papers on electromagnetic one-way edge modes[16,17] concentrated on linear degeneracies, for which the band frequencies near each degeneracy go as $\pm|\vec{\kappa}|$. The reason for looking at linear de-

generacies is that they occur whenever there is no *a priori* reason for the
$O(\kappa)$ term in (4.2) to vanish. The effective Hamiltonian takes the form of a
two-dimensional Dirac Hamiltonian, such as

$$H(\kappa) = \lambda_0 \left(\kappa_x \sigma_1 + \kappa_y \sigma_3 \right), \tag{4.3}$$

where σ_i represent Pauli matrices. These degeneracies are therefore referred
to as "Dirac points"[45].

The degeneracies in the C_{4v} bandstructure shown in Fig. 3.2 are clearly
quadratic, not linear. Therefore, the effective theory based on the two-
dimensional Dirac Hamiltonian does not describe this bandstructure. But
whereas Dirac points have been extensively analyzed in the condensed-matter
literature[45], there has been, to the best of my knowledge, no analogous study
of quadratic degeneracies.

In this chapter, I present an effective theory that describes the bands near
a quadratic degeneracy point, based on the symmetry properties of k-space
around that point. It turns out that the quadratic degeneracy in the C_{4v} crys-
tal can be regarded as a pair of linear degeneracies, analytically continuable
to Dirac points, that are "pinned" to the same k-space point by the crystal
symmetry. The quadratic degeneracy is robust against perturbations such as
variations in the permittivity and radius of the rods, as long as the C_{4v} sym-
metry is preserved. The degeneracy can be lifted by parity and time-reversal
symmetry breaking. In that case, the two bands acquire Chern numbers of

± 1, in agreement with the numerical result of the previous chapter. Breaking the 90° rotational symmetry "unpins" the quadratic degeneracy point, which splits apart into two distinct linear degeneracies. The theory applies to any two-dimensional Bloch system, whether electronic or photonic, with C_{4v} symmetry and a quadratic degeneracy point. In particular, we show that it accurately describes the aforementioned photonic crystal of dielectric rods for a wide range of dielectric contrasts and rod radii.

4.2 Effective Hamiltonian

Suppose we are able to find an effective Hamiltonian $H(\kappa)$ that satisfies (4.2) for the C_{4v} crystal. When the crystal is perturbed, (4.2) should remain valid for some analytical continuation of $H(\kappa)$, even if the perturbation breaks C_{4v}. In other words, although the basis functions $u_0^1(\vec{r})$ and $u_0^2(\vec{r})$ are not $\kappa = 0$ eigenstates of the perturbed system, they remain valid basis functions for the perturbed eigenstates around $\kappa \sim 0$. The mixing elements $c_{nm}(\vec{\kappa})$ shown in (4.1) are altered by the perturbation, and this is reflected in $H(\vec{\kappa})$.

We will be interested in three different symmetry-breaking perturbations of the square lattice. Firstly, we could "shear" the lattice by rotating the basis vectors as follows:

$$
\begin{aligned}
\vec{a}_1 &= a\left(\cos\theta, \sin\theta\right) \\
\vec{a}_2 &= a\left(\sin\theta, \cos\theta\right),
\end{aligned}
\tag{4.4}
$$

where a denotes the lattice constant. This breaks the symmetry under C_4 rotations and reflections about the x and y axes. Secondly, we could distort the rods by stretching them along the x or y axes—or, alternatively, stretching the lattice vectors and rescaling k_x and/or k_y; this breaks the symmetry under rotations and reflections about $y = \pm x$. Thirdly, we could break parity (left-right symmetry). This can be accomplished by adding an imaginary off-diagonal component $\mu_{xy} = i\kappa$ to the permeability tensor, as discussed in the previous chapter.

We will shortly see that breaking parity in this system is equivalent to breaking time-reversal symmetry. For simplicity, we will mostly refer to "parity" instead of "time-reversal symmetry" in this chapter. This is because parity has a direct meaning in the context of the C_4 symmetry group, which we will exploit to construct the effective theory.

We are now ready for the central result of this chapter. I claim that the following effecitve Hamiltonian describes the quadratic degeneracies of a C_{4v} crystal, including the symmetry-breaking effects that we have discussed:

$$H = \lambda_0 \left[\sum_{i=1}^{3} \alpha_i \sigma_i + \beta(\kappa_x^2 - \kappa_y^2)\,\sigma_1 + 2\kappa_x \kappa_y\,\sigma_3 + \gamma |\vec{\kappa}|^2 \right]. \qquad (4.5)$$

This Hamiltonian contains six phenomenological parameters: λ_0, β, γ, and $\alpha_{1,2,3}$. The parameter λ_0 determines the frequency scale, while β and γ control the relative curvatures of bands along different directions. The α parameters determine the strength of the symmetry breaking: α_1 controls

the relative lengths of the two lattice vectors, α_2 is proportional to the parity-breaking permeability component μ_{xy}, and α_3 is proportional to the shear angle θ defined in (4.4).

This Hamiltonian is valid in the neighborhood of $\kappa = 0$, and we have omitted $O(\kappa^4)$ terms which have negligible effects on the band properties in the regime of interest. Furthermore, we assume that the symmetry-breaking is weak (e.g. $\theta \ll 1$), and thus retain only symmetry-breaking terms that are zeroth-order in κ.

In the next two sections, we will determine the bandstructure produced by (4.5), and show that it is consistent with the symmetries of the system. By comparing this bandstructure to the numerically obtained bandstructure, we will then be able to show that (4.5) is an appropriate effective Hamiltonian.

4.3   Bandstructure

When $\alpha_1 = \alpha_3 = 0$, the eigenvalues of (4.5) are

$$\lambda_\pm(\vec{\kappa})/\lambda_0 = \gamma |\vec{\kappa}|^2 \pm \sqrt{|\vec{\kappa}|^4 + (\beta^2 - 1)(\kappa_x^2 - \kappa_y^2)^2 + \alpha_2^2}. \qquad (4.6)$$

Suppose we assume $\beta = 1$ (setting $\beta \neq 1$ simply distorts the bandstructure along the $\kappa_x = \pm \kappa_y$ directions). For $\alpha_2 = 0$, (4.6) then reduces to a pair of quadratic bands $\lambda_\pm/\lambda_0 = (\gamma \pm 1)|\vec{\kappa}|^2$, which meet at $\vec{\kappa} = 0$. The parameter γ controls the relative curvatures of the two bands: for instance, the bands have

equal and opposite curvatures when $\gamma = 0$, whereas they curve in opposite directions with a flatter upper band when $-1 < \gamma < 0$. Two examples of such bands are shown in Fig. 4.1(a) and Fig. 4.1(c).

Setting $\alpha_2 \neq 0$ lifts the degeneracy and opens a bandgap $\Delta\lambda = 2\lambda_0\alpha_2$. The two bands will curve in the *same* direction at $\vec{\kappa} = 0$, as we observed in Fig. 3.2.

Now consider the case where $\alpha_3 \neq 0$, keeping $\alpha_1 = 0$. For $\alpha_2 = 0$, the quadratic degeneracy splits into two distinct degeneracy points, at

$$
\begin{aligned}
\vec{\kappa}_\pm &= \pm(\sqrt{\alpha_3/2}, -\sqrt{\alpha_3/2}) & \text{for } \alpha_3 > 0 \\
\vec{\kappa}_\pm &= \pm(\sqrt{-\alpha_3/2}, \sqrt{-\alpha_3/2}) & \text{for } \alpha_3 < 0.
\end{aligned}
\tag{4.7}
$$

We will henceforth assume that $\alpha_3 > 0$; the following discussion can be easily adapted to the $\alpha_3 < 0$ case. Examples of these linear degeneracies are shown in Fig. 4.1(b) and Fig. 4.1(d).

Let us expand the Hamiltonian around $\vec{\kappa}_\pm$, using the variables

$$
\begin{aligned}
q_1 &= \frac{1}{2}(\kappa_x + \kappa_y) \\
q_2 &= \frac{1}{2}(-\kappa_x + \kappa_y) \pm \sqrt{\alpha_3/2},
\end{aligned}
\tag{4.8}
$$

which are simply k-space displacements from $\vec{\kappa}_\pm$, rotated by $45°$. To first order in q_1 and q_2,

$$
H_\pm(\vec{q})/\lambda_0 \simeq \gamma(\alpha_3 \mp \sqrt{8\alpha_3}\, q_2) \pm \sqrt{8\alpha_3}\,(\beta q_1 \sigma_1 + q_2 \sigma_3) + \alpha_2\, \sigma_2.
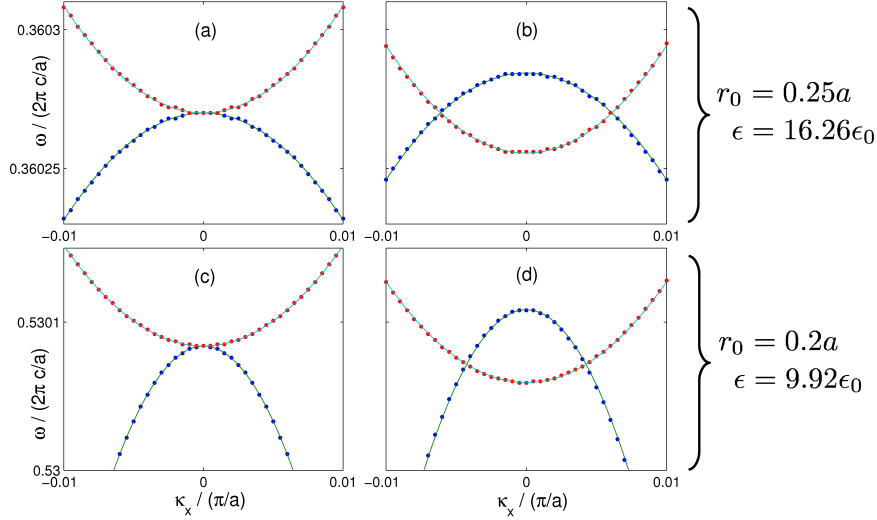\tag{4.9}
$$

Figure 4.1: The second and third TM photonic bands for time-reversible lattices of dielectric rods, plotted against κ_x, where $\vec{\kappa} = (\kappa_x, -\kappa_x)$ (i.e. along the line ΓM). Note that the effective Hamiltonian (4.5) is independent of β along this line. The rods have radius r_0 and permittivity ϵ, where $r_0 = 0.25a$ and $\epsilon = 16.26$ for (a) and (b), and $r_0 = 0.25a$ and $\epsilon = 16.26$ for (c) and (d). Dots show numerical data (generated using MPB[50]); solid lines show analytic results after fitting the parameters in (4.5) to the numerical data. In (a) and (c), the square lattice is undistorted ($\theta = 0$ and $\alpha_3 = 0$), and there is a quadratic degeneracy at $\kappa = 0$. In (b) and (d), the lattice is sheared by an angle θ: (b) $\theta = 1.2 \times 10^{-4}$ radians, with fitted value $\alpha_3 = 3.7 \times 10^{-5}(\pi/a)^2$; (d) $\theta = 10^{-4}$ radians, with fitted value $\alpha_3 = 1.8 \times 10^{-5}(\pi/a)^2$. The quadratic degeneracy then splits into two linear degeneracies.
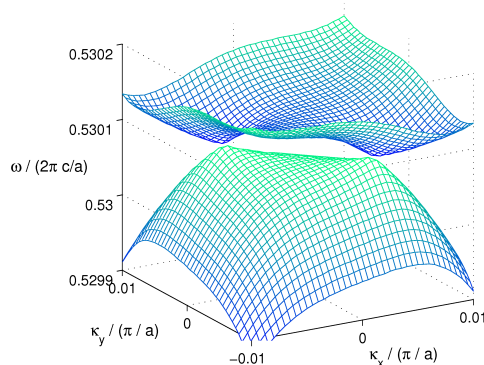
Figure 4.2: Three-dimensional plot for the bandstructure of Fig. 4.1(d), showing the distorted Dirac spectrum.

When $\gamma = 0$ and $\beta = 1$, this reduces to a two-dimensional Dirac Hamiltonian near each each degeneracy point (or "Dirac point"). Furthermore, α_2 plays the role of a mass term, opening a bandgap $\Delta\lambda = 2\lambda_0\alpha_2$. Setting $\gamma \neq 0$ distorts the Dirac Hamiltonian and its eigenvalue spectrum: as shown in Fig. 4.1(d), the Dirac cones in the $\alpha_2 = 0$ limit are "tilted" in k-space.

Along the line $\kappa_y = \pm\kappa_x$, the splitting of the degeneracy point can be thought of as a vertical relative displacement of the two parabolic bands. Note, however, that the bands meet only at isolated points in the full κ-space, as shown in Fig. 4.2. The splitting is accompanied by a change in the density of states from a discontinuity to a linear "dip" centered at the frequency of the band degeneracy. When $\alpha_2 \neq 0$, the density of states is discontinuous at the band edges, dropping to zero inside the band gap. (For photonic crystals, this refers to the density of states for either TE or TM modes, not the entire photonic density of states.)

The situation is very similar for $\alpha_1 \neq 0$. When $\alpha_2 = \alpha_3 = 0$, the degeneracy splits into two, but along the line $\kappa_y = 0$ (if $\alpha_1 > 0$) or $\kappa_x = 0$ (if $\alpha_1 < 0$), instead of $\kappa_x = \pm\kappa_y$. When both α_1 and α_3 are nonzero, the degeneracies are located at an intermediate location, $\kappa_\pm = \pm(\alpha_1^2 + \alpha_3^2)^{1/4}(\cos\phi, \sin\phi)$, where $\tan\phi = \alpha_3/\alpha_1$, and expanding around each point yields a Dirac-like Hamiltonian analogous to (4.9).

When $\alpha_2 \neq 0$, the bands are non-degenerate, and their Chern numbers can be calculated. The details of this calculation are given in Appendix B. The result is that the upper and lower bands possess Chern numbers $-\text{sgn}(\alpha_2)$ and $\text{sgn}(\alpha_2)$ respectively, regardless of the values of α_1, α_3, β, and γ. This implies the existence of a single family of one-way edge modes[43], and agrees exactly with the numerical results of the previous chapter.

Although the effective Hamiltonian (4.5) is only valid near $\kappa = 0$, it yields the same Chern number as the actual bandstructure because only the region near the broken degeneracy point provides a non-vanishing "Berry flux" contribution to the Chern number, as explained in Appendix A. Furthermore, while our theory only describes weak symmetry-breaking, the Chern number is a topological quantity and cannot be altered by non-perturbative distortions, as long as the bands remain non-degenerate. Therefore, it remains unchanged even in the strong parity-breaking regime explored in the previous chapter.

When α_1 and/or α_3 are non-zero, the two linear degeneracy points each contribute $\pm 1/2$ to the Chern number, in accordance with previous analyses

of the Dirac Hamiltonian[45]. When $\alpha_1 = \alpha_3 = 0$, the Berry connection winds twice as fast around the point $\kappa = 0$, which provides the entire contribution of ± 1. The dependence of the Chern number on the sign of α_2 confirms that α_2 controls parity breaking, since the Chern number can be shown to vanish identically when parity is unbroken.

4.4 Symmetry properties

The fully symmetric Hamiltonian $H_0 \equiv H|_{\alpha_i = 0}$ must transform under any operation $g \in C_{4v}$ as

$$D(g)H_0(\vec{\kappa})D^{-1}(g) = H_0(g\vec{\kappa}). \tag{4.10}$$

The matrices $D(g)$ form a two-dimensional representation of C_{4v}. It is easy to verify that (4.10) holds if and only if $D(g)$ falls under the two-dimensional irreducible representation conventionally denoted as $\chi^{(5)}$, which is also the only two-dimensional irreducible representation for C_{4v}[51]. The representation is shown in Table 4.1. The transformation properties of the symmetric Hamiltonian are unaffected by the parameters β, γ, or λ_0.

By studying how $H(\vec{\kappa})$ transforms under this group representation, we can show that the quadratic degeneracy is protected by the crystal symmetry. Any zeroth-order term proportional to the identity matrix, when added to H_0, simply shifts the eigenvalues without opening a gap. Adding a zeroth-

g	Description	$D(g)$
E	Identity	1
C_4	90° clockwise rotation	$\begin{bmatrix} 0 & 1 \\ -1 & 0 \end{bmatrix} = i\sigma_2$
C_4^3	90° anticlockwise rotation	$\begin{bmatrix} 0 & -1 \\ 1 & 0 \end{bmatrix} = -i\sigma_2$
C_4^2	180° rotation	-1
m_x	Reflection about κ_x-axis	$\begin{bmatrix} 0 & 1 \\ 1 & 0 \end{bmatrix} = \sigma_1$
m_y	Reflection about κ_y-axis	$\begin{bmatrix} 0 & -1 \\ -1 & 0 \end{bmatrix} = -\sigma_1$
σ_u	Reflection about $\kappa_y = \kappa_x$	$\begin{bmatrix} 1 & 0 \\ 0 & -1 \end{bmatrix} = \sigma_3$
σ_v	Reflection about $\kappa_y = -\kappa_x$	$\begin{bmatrix} -1 & 0 \\ 0 & 1 \end{bmatrix} = -\sigma_3$

Table 4.1: Representation for the symmetry transformations of C_{4v} acting on the effective Hamiltonian (4.5). This is the only two-dimensional irreducible representation of C_{4v}, up to the usual similarity transformations[51].

order term proportional to σ_1 (i.e. $\alpha_1 \neq 0$) breaks C_{4v} since, under the representation given in Table 4.1, $\alpha \to -\alpha$ for 90° rotations and reflections across $\kappa_x = \pm \kappa_y$. Note that $\alpha \to \alpha$ for reflections across the κ_x and κ_y axes, in agreement with our claim that $\alpha_1 \neq 0$ corresponds to stretching the lattice. Similarly, setting $\alpha_2 \neq 0$ preserves the rotational symmetries but breaks the reflection symmetries (parity). Finally, setting $\alpha_3 \neq 0$ preserves the reflection symmetry across $\kappa_x = \pm \kappa_y$ but breaks the symmetry under 90° rotations and reflections across $\kappa_x = 0$ and $\kappa_y = 0$.

Furthermore, the Hamiltonian cannot include terms that are first-order in $\vec{\kappa}$ if the C_{4v} symmetry is unbroken or only partially broken. Such terms have the general form

$$\Delta H = \sum_{i=1}^{2} \sum_{j=1}^{3} \kappa_i c_{ij} \sigma_j, \tag{4.11}$$

and we can show that $c_{ij} = 0$ for all i, j as long as the system is symmetric under either rotations, reflections about the κ_x and κ_y axes, or reflections about $\kappa_x = \pm \kappa_y$. At least one of these symmetries is preserved by each of the three "elementary" distortions discussed above. For example, suppose we break parity while leaving the system rotationally invariant. According to Table 4.1, 90° anticlockwise rotations are represented by $-i\sigma_2$, so

$$\sigma_2 \Delta H(\kappa_x, \kappa_y) \sigma_2 = \Delta H(-\kappa_y, \kappa_x). \tag{4.12}$$

Inserting (4.11) into both sides of this equation, we obtain the following six

equations for the coefficients c_{ij}:

$$\begin{aligned}
-c_{11} &= c_{21}, & c_{12} &= c_{22} \\
-c_{13} &= c_{23}, & -c_{11} &= -c_{21} \\
c_{12} &= -c_{22}, & -c_{13} &= -c_{23}
\end{aligned} \tag{4.13}$$

The only possible solution is $c_{ij} = 0$ for all i, j.

This situation may be contrasted with a triangular or honeycomb lattice, for which there is a C_{3v} symmetry around each corner of the hexagonal Brillouin zone. There, one can write down an $O(\kappa)$ Hamiltonian which transforms under a two-dimensional irreducible representation of C_{3v}: this is just the Dirac Hamiltonian (4.3). In that case, a zeroth-order "mass" term proportional to σ_2 controls parity breaking[45].

4.5   Comparison with numerical results

We can check the validity of the ansatz (4.5) by comparing its bandstructure to numerical results. In this section, I will use results obtained using the MPB[50] and COMSOL[47] computer programs, which solve the Maxwell equations without any approximations apart from the discretization of the simulation cell.

Let us begin with the fully-symmetric crystal, for which $\alpha_1 = \alpha_2 = \alpha_3 = 0$. We can determine β and γ by fitting the effective bandstructure (4.6) to numerical bandstructures. Fig. 4.3 shows the results of least-squares fits for

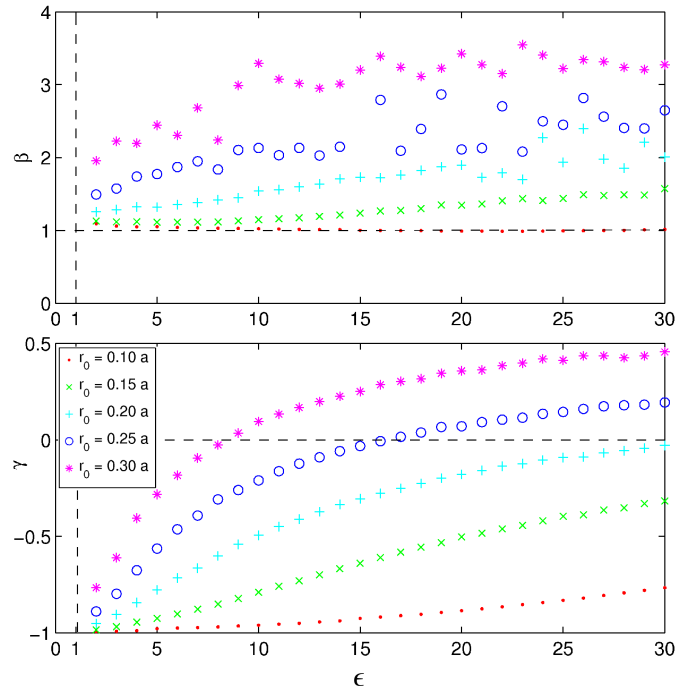Figure 4.3: Values of β and γ obtained from least-squares fits of (4.6) to bandstructures computed numerically along the lines $k_y = \pi/a$ and $k_x = -k_y$. The photonic crystal consists of a square lattice of rods with radius r_0 and permittivity ϵ, embedded in air.

a variety of rod radii r_0 and permittivities ϵ. Two typical fits are shown in Fig. 4.1(a) and Fig. 4.1(c). We find that β and γ are both strongly dependent on r_0 and ϵ.

In all these simulations, we will assume that $\mu_{xx} = \mu_{yy} = \mu_0$, in order to avoid introducing an additional numerical parameter. If we set μ_{xx} and μ_{yy} to, say, the values for the YIG crystal studied in Chapter 3, that introduces a different set of best-fit parameters. However, the main conclusions in this chapter are unaltered.

When the simulated crystal is perturbed by changing the lattice constant slightly along (say) the x direction ($\delta a_x < 0$), the degeneracy splits along the line $\kappa_y = 0$ in the computed bandstructures. From the location of the linear degeneracies, we can obtain α_1. Similarly, shearing the lattice by an angle $\theta \neq 0$ induces linear degeneracies along the line $\kappa_x = \kappa_y$, as shown in Fig. 4.1(b) and Fig. 4.1(d), and this yields α_3. Finally, we can obtain α_2 by introducing an off-diagonal permeability component $\mu_{xy} = i\kappa$ in the rods and fitting the resulting bandstructure to (4.6).

We find that that α_1 is proportional to δa_x, α_2 is proportional to κ, and α_3 is proportional to θ, as shown in Fig. 4.4. Like β and γ, the proportionality factors $\alpha_1/\delta a_x$, α_2/κ, and α_3/θ depend on r_0 and ϵ. In other words, the positions of the linear degeneracies induced by shearing and/or stretching the lattice do not depend solely the lattice geometry, but also on the underlying details of the crystal. This behavior differs from that of previously-studied Dirac points in triangular and hexagonal lattices, where, as we have seen, the
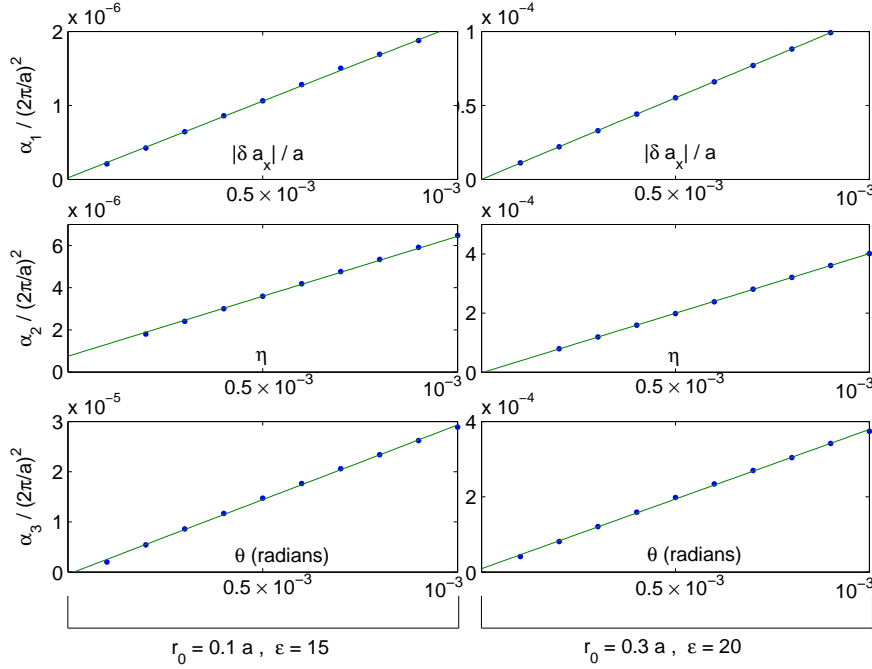
Figure 4.4: Plots of α_1, α_2, and α_3 for two different photonic crystals of dielectric rods with radius r_0 and permittivity ϵ. In the left column, the dielectric rods have radius $r_0 = 0.1a$ (where a is the lattice constant) and permittivity $\epsilon = 15$. In the right column, $r_0 = 0.3a$ and $\epsilon = 20$. We obtain α_1 from the location of the degeneracies $\vec{\kappa} = \pm(0, \sqrt{\alpha_1/\beta})$ for lattice stretching parameter $\delta a_x/a$. We obtain α_2 by performing a nonlinear least-squares fit of Eq. (4.6) to the computed $\mathcal{T}$-broken bandstructures along the line $\kappa_x = -\kappa_y$, using the values of γ found in Fig. 4.3 (which were obtained using the symmetric lattice); it is plotted against the imaginary off-diagonal permeability component, $\mu_{xy} = i\kappa$. We obtain α_3 from the location of the degeneracies $\vec{\kappa} = \pm(\sqrt{\alpha_3/2}, -\sqrt{\alpha_3/2})$, for lattice distortion angle θ.

Dirac points are invariably pinned to the corners of the hexagonal Brillouin zone by the C_{3v} symmetry.

Fig. 4.5 compares the numerically computed bandstructure of a parity-broken photon crystal with the effective bandstructure, utilizing the parameters obtained above. Here, we use the values of λ_0, β, and γ computed for the parity-symmetric system, and the proportionality constant α_2/κ found above. In this sense, the effective bandstructure is "predicted" and not directly fitted to the numerical data. As we can see, the theory matches the numerical results very well within its region of validity ($\kappa \sim 0$).

4.6   Implications of the effective theory

In the preceding section, we have seen that the effective Hamiltonian (4.5) accurately describes the bands of a C_{4v} photonic crystal in the vicinity of a band degeneracy. I would like to point out, in closing, that the effective theory should be applicable to *any* electronic or photonic system possessing C_{4v} symmetry and a two-fold band degeneracy, regardless of the other physical details of the system. In particular, the various results obtained in section 4.4 must hold based on symmetry considerations alone. This includes the protection of the quadratic nature of the degeneracy, the forbidding of linear degeneracies, and the Chern numbers induced by parity breaking.

As an example of an electronic system for which (4.5) is a valid effective Hamiltonian, consider a tight-binding model shown in Fig. 4.6, which consists
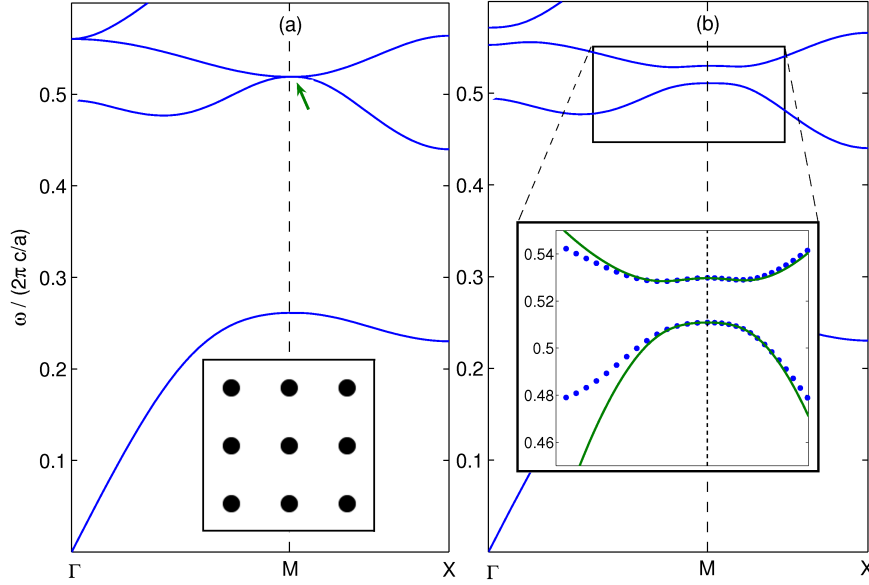
Figure 4.5: TM bandstructure of a two-dimensional photonic crystal formed by a square lattice of dielectric rods. (a) Fully symmetric crystal with rod radius $0.15a$ (where a is the lattice constant) and $\epsilon = 20\epsilon_0$. The rods are embedded in air, and $\mu = 1$ everywhere. The quadratic degeneracy between the second and third TM bands is indicated with an arrow. Inset: the crystal structure in real space. (b) Parity-broken crystal, with off-diagonal permeability component $\mu_{xy} = 0.1i$ in the rods. Inset: Band structure near the lifted degeneracy, with dots showing numerical solutions of the exact Maxwell equations[47]. The solid lines show the analytic approximation of (4.6), where λ_0, β, and γ are calculated from the symmetric system and α_2 is calculated separately based on the proportionality constant with $|\mu_{xy}|$ (see Fig. 4.4.)
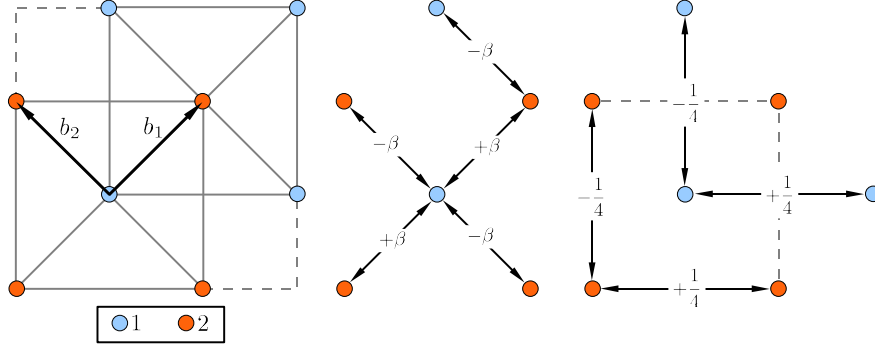
Figure 4.6: A tight-binding model that is described by the effective Hamiltonian (4.5) near $k = 0$.

of two interleaved square lattices with d-wave hopping between nearest and next-nearest neighbors. If we denote the creation operators on sublattices 1 and 2 as $a^\dagger$ and $b^\dagger$, and the nearest-neighbor lattice vectors as b_1 and b_2, the tight-binding Hamiltonian is

$$
\begin{aligned}
H = \sum_f & \left\{ \frac{1}{4} \left[\left(-a^\dagger_{r+b_1+b_2} + a^\dagger_{r+b_1-b_2} \right) a_r + \left(b^\dagger_{r+2b_1+b_2} - b^\dagger_{r+2b_1-b_2} \right) b_{r+b_1} \right] \right. \\
& \left. + \beta \left[\left(-b^\dagger_{r+b_1} + b^\dagger_{r+b_2} \right) a_r + \left(-a^\dagger_{r+2b_1} + a^\dagger_{r+b_1+b_2} \right) b_{r+b_1} \right] \right\} \\
& + \text{h.c.}
\end{aligned}
$$

$$(4.14)$$

As usual, this can be solved by Fourier-transforming the fermion operators

to obtain a Fourier decomposition $H = \sum_k H_k$. For $k \sim 0$, we find that

$$H_k = b^2 \begin{bmatrix} a_k \\ b_k \end{bmatrix}^\dagger \begin{bmatrix} k_1 k_2 & \beta \left(k_1^2 - k_2^2 \right) \\ \beta \left(k_1^2 - k_2^2 \right) & -k_1 k_2 \end{bmatrix} \begin{bmatrix} a_k \\ b_k \end{bmatrix} + O(k^3), \qquad (4.15)$$

which is the desired effective Hamiltonian. In this system, β regulates the strength of nearest neighbor hopping between the two sublattices as compared to the strength of next-nearest-neighbor hopping within each sublattice. In this light, the existence of a free β variable dependent on the underlying physical properties of the lattice is unsurprising. It should be pointed out, however, that this tight-binding model is not generally applicable to photonic crystals, since most photonic Bloch modes are poorly-localized; I am simply presenting it as an illustration that the effective Hamiltonian (4.5) and its associated behaviors could show up in other physical contexts. Indeed, a similar effective Hamiltonian has previously been found by Onoda and Nagaosa[52], while studying a tight-binding model of a two-dimensional square-lattice ferromagnet.

Degeneracy points occuring in lattices with fundamental symmetries different from C_{4v} can be studied via a program similar to the one outlined in this chapter. As long as the degeneracy occurs at a point with a high degree of symmetry, that symmetry can be exploited, by guessing an appropriate representation of the symmetry group, to yield the most general possible form of the effective Hamiltonian. The advantage of this procedure is that it

relies only on symmetry principles, and can therefore be applied when other methods, such as tight-binding, are not readily applicable.

Conclusions

In this thesis, I have studied two types of photonic crystals which break the conventional mold in very different ways.

The first type consists of systems in which the scattering centers of the "photonic crystal" are single atoms interacting with the electromagnetic field via an optical resonance. We saw that quantum mechanical polariton theories, coupled with band-theoretical arguments, can yield intuitive explanations for the behavior of these systems, such as the resonant enhancement of the photonic bandgap and the dependence of the dark state polariton's group velocity on the control beam.

The second type of unconventional photonic crystal breaks time-reversal symmetry by incorporating magneto-optic materials, leading to topologically distinct bandstructures (i.e., bands possessing non-zero Chern numbers). We have seen that these systems give rise to the peculiar phenomenon of one-way edge modes, and that it is feasible to observe these modes experimentally. Much work remains to be done on this topic; in particular, it will be interesting—especially from the technological applications point of view—to

find a method for generating one-way edge modes at terahertz, or higher, frequencies.

Appendix A

Chern numbers and topology

The effect of time-reversal symmetry breaking on Bloch systems, such as photonic crystals, can be summarized by a mathematical quantity known as the Chern number or TKNN number[40]. This was introduced into physics by Thouless, Kohmoto, Nightingale, and den Nijs in 1982, in their seminal study of quantum Hall systems in a periodic scalar potential. Non-zero Chern numbers are associated with a variety of interesting physical phenomena, particularly unidirectional edge states—called chiral edge states in quantum Hall systems, or one-way edge modes in photonic crystals. This Appendix provides a self-contained overview of the relevant mathematical background.

Consider a time-independent Schrödinger equation,

$$\mathcal{H}(r)\,\psi(r) = E\psi(r). \tag{A.1}$$

The eigenfunctions $\psi(r)$ might be scalars, vectors, spinors, or more compli-
cated objects. In this thesis, we are interested in the Hermitian form of the
classical Maxwell equations, where, as shown in (3.7), ψ is the electric field
vector and

$$\mathcal{H} = \epsilon^{-1} \nabla \times \left(\boldsymbol{\mu}^{-1}(r) \nabla \times \cdot \right). \tag{A.2}$$

Suppose $\mathcal{H}(r)$ is periodic in the x-y plane, with periodic boundary con-
ditions and a total of N unit cells. We assume there is no z-dependence, so
that the problem is two-dimensional. Bloch's theorem states that the eigen-
functions can be uniquely labelled by two quantum numbers (n, k), where n
an integral band index and k is a wavevector in the first Brillouin zone:

$$\psi_{nk}(r) = \frac{1}{\sqrt{N}} u_{nk}(r) e^{ik \cdot r}. \tag{A.3}$$

The Bloch function $u_{nk}(r)$ has the periodicity of the Hamiltonian and obeys
a modified Schrodinger equation

$$\mathcal{H}_k(r) u_{nk}(r) = E_{nk} u_{nk}(r), \tag{A.4}$$

where $\mathcal{H}_k$ is obtained by substituting (A.3) into (A.1), i.e. replacing ∇ with
$\nabla + ik$. We can refer to abstract kets $|nk\rangle$ instead of Bloch functions $u_{nk}(r) = \langle r|nk\rangle$. The Bloch functions obey the orthonormality condition

$$\langle nk|n'k\rangle = \int_\Omega d^2r \, u^*_{nk}(r) u_{n'k}(r) = 1, \tag{A.5}$$

where Ω denotes the area of the unit cell.

For the prototypical quantum Hall system—a two-dimensional electron gas in a uniform magnetic field—there is an additional complication: the vector potential that gives rise to a uniform magnetic field is not periodic under ordinary lattice translations, so neither is the Hamiltonian. This problem is skirted by introducing the concepts of "magnetic translations" and "magnetic Bloch functions" [40]. I will not discuss this complication here, as it does not affect the subject of this thesis. The electromagnetic Hamiltonian (A.2) is periodic under ordinary lattice translations.

For each band n, the Chern number (or TKNN number) [40] C_n is defined as the following integral:

$$C_n = \frac{1}{2\pi i} \int_{BZ} d^2k \int_{\Omega} d^2r \; \left(\frac{\partial u^*_{nk}}{\partial k_x} \frac{\partial u_{nk}}{\partial k_y} - \frac{\partial u^*_{nk}}{\partial k_y} \frac{\partial u_{nk}}{\partial k_x} \right). \qquad \text{(A.6)}$$

This is an area integral carried out in both k-space and real space, over the first Brillouin zone and the real-space unit cell respectively.

The Chern number C_n is a measure of certain topological characteristics of a band, and is completely unaffected by sufficiently weak changes in $\mathcal{H}$ (the precise meaning of "sufficiently weak" will eventually become clear). This relies on the fact, which we shall shortly prove, that C_n is always an integer, and it is impossible to go continuously from one integer to another. In other words, suppose we start with a Hamiltonian $\mathcal{H}(r)$ whose eigenfunctions are grouped into bands $n = 1, 2, \cdots$ possessing Chern numbers $C_1, C_2, \cdots$. If

we continuously tune the parameters of $\mathcal{H}$, such as particle masses or the strengths of external fields, the Bloch functions and their eigenvalues vary continuously in some complicated way. However, the Chern numbers remain completely unchanged, until we tune past some critical value. At that point, they change abruptly to some other set of integers $C_1{}', C_2{}', \cdots$.

We will now prove that the Chern number is always an integer. For each (n, k), define the following k-space vector, known as the Berry connection:

$$\vec{\mathcal{A}}^{nn'}(k) = \int_\Omega d^2r \; u_{nk}^*(r) \nabla_k u_{n'k}(r) = \langle nk | \nabla_k | n'k \rangle . \tag{A.7}$$

Here, $\nabla_k \equiv (\partial/\partial k_x, \partial/\partial k_y)$. In terms of the Berry connection, we can write (A.6) as

$$\begin{aligned}
C_n &= \frac{1}{2\pi i} \int_{BZ} d^2k \; \left(\frac{\partial \mathcal{A}_y^{nn}}{\partial k_x} - \frac{\partial \mathcal{A}_x^{nn}}{\partial k_y} \right) \\
&= \frac{1}{2\pi i} \int_{BZ} d^2k \; (\nabla_k \times \vec{\mathcal{A}}^{nn}(k)) \cdot \hat{z}.
\end{aligned} \tag{A.8}$$

According to Stokes' theorem, the flux of a curl through a surface can be re-expressed as a line integral around the edge of the surface. This implies that the above integral is equal to the following line integral around the boundary of the Brillouin zone:

$$C_n \stackrel{?}{=} \frac{1}{2\pi i} \oint_{\partial(BZ)} d\vec{k} \cdot \vec{\mathcal{A}}_{nn}(k). \tag{A.9}$$
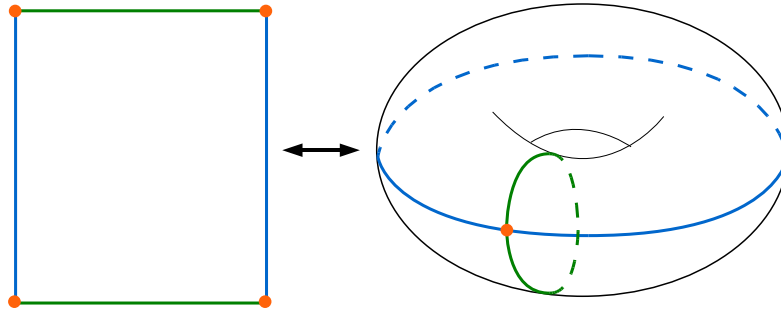
Figure A.1: The Bloch functions are defined in the first Brillouin zone with periodic boundary conditions. The Brillouin zone is therefore topologically equivalent to a torus.

This appears to vanish since the Bloch functions (and the Berry connection $\mathcal{A}(k)$) are defined smoothly and periodically in the Brillouin zone. The contributions to the integral from opposite ends of the zone should cancel.

Another way to say this is that the Brillouin zone is topologically equivalent to the surface of a torus, as shown in Fig. A.1. Therefore, (A.9) is equivalent to the flux (of a curl) through the entire surface of the torus. Since the surface of the torus has no boundary, the flux is zero. We can see this by noting that Stoke's theorem equates the flux integral to a line integral carried out along an infinitesimal loop residing on the suface (since the theorem is agnostic about which side of the loop we take as the flux integral, the flux through the infinitesimal area of the loop is the negative of the flux through the entire remaining surface of the torus). This vanishes since the area of the loop is infinitesimal.

The crucial loophole in this reasoning was pointed out by Kohmoto[42]. It

is sometimes impossible to define the Bloch functions smoothly and uniquely over the entire Brillouin zone due to the existence of *phase singularities*. Suppose we have a set of eigenstates $|nk\rangle$ that solve (A.4). This set is not uniquely defined, as we can multiply each $|nk\rangle$ by an arbitrary phase factor $\exp[i\phi(k)]$, where $\phi(k)$ is real and periodic in the Brillouin zone. Generally, we attempt to choose $\phi(k)$ such that, for an arbitrary fixed value of r, the resulting Bloch function $u_{nk}(r)$ varies continuously with k over the entire Brillouin zone. A phase singularity occurs if this scheme fails at any isolated point k_0 in the Brillouin zone: for neighboring $k \approx k_0$,

$$|nk\rangle \approx e^{ip\,\mathrm{arg}(k-k_0)}|k_0\rangle,\ p \in \mathbb{Z}. \tag{A.10}$$

Here, $\mathrm{arg}(k - k_0)$ is the angle of $k - k_0$ relative to the k_x axis. Kohmoto showed that in a quantum Hall system, can always find at least one point k_0 that satisfies this condition, for any given value of r.

For a given set of phase singularities in the Brillouin zone, the Chern number (A.8) is the sum of line integrals around infinitesimal k-space loops enclosing each singularity. For each singularity,

$$\frac{1}{2\pi i}\oint_{k_0} d\vec{k}\cdot\langle nk|\nabla_k|nk\rangle = p \in \mathbb{Z}, \tag{A.11}$$

where p is the winding number defined in (A.10). We have thus proven that the Chern number is an integer.

There is an important relationship between Chern numbers and band de-

generacies, which was first pointed out by Simon[41]. By resolving the identity, we can write (A.8) as

$$
C_n = \frac{-1}{2\pi i} \sum_{n'} \int_{BZ} d^2k \left(\left\langle nk \left| \frac{\partial}{\partial k_x} \right| n'k \right\rangle \left\langle n'k \left| \frac{\partial}{\partial k_y} \right| nk \right\rangle \right.
$$
$$
\left. - \left\langle nk \left| \frac{\partial}{\partial k_y} \right| n'k \right\rangle \left\langle n'k \left| \frac{\partial}{\partial k_x} \right| nk \right\rangle \right). \quad \text{(A.12)}
$$

Using the "Feynman-Hellman" theorem

$$
\langle nk|\partial\mathcal{H}/\partial k_i|n'k\rangle = (E_{n'k} - E_{nk}) \langle nk|\partial/\partial k_i|n'k\rangle + \frac{\partial E_{nk}}{\partial k_i}\delta nn', \quad \text{(A.13)}
$$

this becomes

$$
C_n = \frac{1}{2\pi i} \sum_{n'} \int_{BZ} d^2k \left[\left\langle nk \left| \frac{\partial\mathcal{H}_k}{\partial k_x} \right| n'k \right\rangle \left\langle n'k \left| \frac{\partial\mathcal{H}_k}{\partial k_y} \right| nk \right\rangle \right.
$$
$$
\left. - \left\langle nk \left| \frac{\partial\mathcal{H}_k}{\partial k_y} \right| n'k \right\rangle \left\langle n'k \left| \frac{\partial\mathcal{H}_k}{\partial k_x} \right| nk \right\rangle \right]
$$
$$
\left/ \left[(E_{nk} - E_{n'k})^2 \right] . \quad \text{(A.14)} \right.
$$

We have seen that the Brillouin zone is topologically equivalent to the surface of a torus. Imagine smoothly interpolating $\mathcal{H}_k$ off this surface and into the surrounding three-dimensional space. Suppose that the band n is degenerate with some other band n' for some $k = k_0$ in the three-dimensional space. Generally, this occurs at an isolated k-space point (rather than a line, sheet, or volume)[53]. According to (A.14), such degeneracy points act as
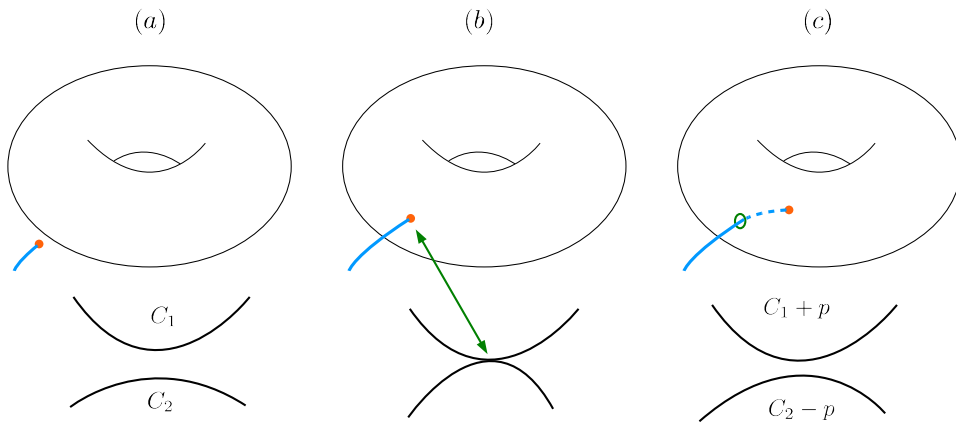
Figure A.2: Relationship between Chern numbers and degeneracies. (a) Initially, a pair of bands have Chern numbers C_1 and C_2. In the extended k-space, there is a degeneracy point, represented by an orange dot, outside the torus whose surface represents the first Brillouin zone. (b) Tuning $\mathcal{H}$ moves the degeneracy onto the torus surface, and it becomes physical. (b) Further tuning moves the degeneracy inside the torus. The Chern numbers are now $C_1 + p$ and $C_2 - p$, where $p \in \mathbb{Z}$. The Bloch functions defined on the torus surface possess a phase singularity with winding number p.

point sources for an abstract flux passing through the torus surface[54]. If we tune parameters in $\mathcal{H}_k$ (other than k itself), the degeneracy points will generally move around in the extended k-space. If k_0 lies outside the torus, the abstract flux sums to zero, so its contribution to the Chern number is zero. If k_0 lies within the torus, it contributes a non-zero integer to both C_n and $C_{n'}$. In fact, according to (A.14) its contributions to C_n and $C_{n'}$ are equal and opposite in sign. Thus, the Chern numbers jump abruptly whenever a degeneracy point pops into or out of the torus, i.e. whenever we tune past a *physical* band degeneracy. This is summarized in Fig. A.2.

The extended k-space degeneracy points are closely-related with the phase singularities discussed earlier, but it is important not to confuse the two. The former are definite points in extended k-space, outside the physical Brillouin zone; the latter reside on the physical Brillouin zone, but their position can be shifted around by an appropriate choice of phase convention. One way to think about this is to imagine strings attached to each degeneracy point, extending to infinity (akin to "Dirac strings" in the theory of magnetic monopoles). The intersection of the string with the surface of the torus is a phase singularity. As long as a degeneracy point lies inside the torus, there is at least one phase singularity on the surface. The Chern number measures the "charge" carried by degeneracy points within the torus, or, equivalently, the total "vorticity" carried by the strings penetrating the torus' surface.

Finally, we note that the Chern number vanishes whenever the Hamiltonian $\mathcal{H}$ obeys time-reversal or parity symmetry. Time-reversal symmetry

implies the following identity for the Bloch functions:

$$u_{nk}(r) = \pm u^*_{n,-k}(r). \tag{A.15}$$

In that case, the Berry connection obeys

$$\mathcal{A}^{nn'}(k) = \mathcal{A}^{nn'}(-k). \tag{A.16}$$

Parity, on the other hand, implies that

$$u_{n(k_x,k_y)}(x, y) = \pm u_{n,(k_x,-k_y)}(x, -y), \tag{A.17}$$

so

$$\begin{aligned}
\mathcal{A}^{nn'}_x(k_x, k_y) &= -\mathcal{A}^{nn'}_x(k_x, -k_y) \\
\mathcal{A}^{nn'}_y(k_x, k_y) &= \mathcal{A}^{nn'}_y(k_x, -k_y).
\end{aligned} \tag{A.18}$$

Upon substituting either (A.16) or (A.18) into (A.8), we find that $C_n = 0$.

Appendix B

Chern numbers for quadratic degeneracies

In this Appendix, we calculate the Chern numbers of the bands associated with the effective Hamiltonian studied in Chapter 4:

$$H = \lambda_0 \left[\sum_{i=1}^{3} \alpha_i \sigma_i + \beta(\kappa_x^2 - \kappa_y^2)\,\sigma_1 + 2\kappa_x\kappa_y\,\sigma_3 + \gamma|\vec{\kappa}|^2 \right]. \qquad \text{(B.1)}$$

We will consider the lower band $|\psi^-(\vec{\kappa})\rangle$; the calculation for the upper band proceeds analogously. First, consider $\alpha_1 = \alpha_3 = 0$. The eigenvectors of (B.1) do not depend on γ since that parameter multiplies the identity matrix. For simplicity, we set $\beta = 1$. Adopting cylindrical coordinates (κ, ϕ), defined as usual by $\kappa_x = \kappa\cos\phi$ and $\kappa_y = \kappa\sin\phi$, we find that the eigenvector

corresponding to the lower band is

$$|\psi^-(\vec{\kappa})\rangle = \frac{1}{\sqrt{2[\kappa^4 + \alpha_2^2 + \kappa^2\sqrt{\kappa^4 + \alpha_2^2}\,\sin 2\phi]}}$$

$$\times \begin{bmatrix} -\kappa^2\cos 2\phi + i\alpha_2 \\ \kappa^2\sin 2\phi + \sqrt{\kappa^4 + \alpha_2^2} \end{bmatrix}. \quad \text{(B.2)}$$

This result is independent of γ. The Berry connection, defined in (A.7), is

$$\vec{\mathcal{A}}^-(\vec{\kappa}) = \frac{i\alpha_2\kappa\left(\cos 2\phi\,\hat{\kappa} - \sin 2\phi\,\hat{\phi}\right)}{\kappa^4 + \alpha_2^2\sqrt{\kappa^4 + \alpha_2^2}\,\sin 2\phi}. \quad \text{(B.3)}$$

To obtain the Chern number, integrate (B.3) around a loop $\kappa = \kappa_0$:

$$\begin{aligned} C^- &= \frac{1}{2\pi i}\oint_{\kappa=\kappa_0} d\vec{\kappa}\cdot\vec{\mathcal{A}}^-(\kappa) \\ &= -\frac{2\alpha_2}{\pi}\int_{-\frac{\pi}{4}}^{\frac{\pi}{4}} \frac{\kappa_0^2\sin 2\phi\,d\phi}{\kappa_0^4 + \alpha_2^2 + \kappa_0^2\sqrt{\kappa_0^4 + \alpha_2^2}\,\sin 2\phi}. \end{aligned} \quad \text{(B.4)}$$

The integral can be performed via the substitution $\sin 2\phi = \tanh u$, and we find that

$$\begin{aligned} C^- &= \text{sgn}(\alpha_2) - \frac{\alpha_2}{\sqrt{\kappa_0^4 + \alpha_2^2}} \\ &\to \text{sgn}(\alpha_2) \text{ for } |\alpha_2| \ll \kappa_0^2. \end{aligned} \quad \text{(B.5)}$$

As discussed in Chapter 4, this result remains unchanged even when we enter the non-perturbative regime, even though our effective theory is only valid

for small values of κ and α_i.

When α_1 and/or α_3 are non-zero, the band maximum at $\kappa = 0$ splits into two distinct maxima, and expanding around each maximum yields a Dirac-like Hamiltonian. For instance, when $\alpha_1 = 0$ and $\alpha_3 \neq 0$ the maxima occur at $\vec{\kappa}_{\pm} = \pm(\sqrt{\alpha_3/2}, -\sqrt{\alpha_3/2})$, and the Hamiltonian near each of these points is given by (4.9). In terms of the variables q_1 and q_2 defined in (4.8), the Berry connection for the lower band is

$$\vec{\mathcal{A}}_{\pm}^{-}(\vec{q}) = \pm \frac{ib}{2} \cdot \frac{\cos\phi\,\hat{q} + \sin\phi\,\hat{\phi}}{q^2 + b^2 \pm q\sqrt{q^2 + b^2}\sin\phi}, \tag{B.6}$$

where $b \equiv \alpha_2/\sqrt{\alpha_3}$, $\pm$ refers to which maximum we are expanding around, and (q, ϕ) is the cylindrical coordinate representation of $\vec{q}$. This Berry connection has the same form as (B.3), but winds half as quickly around each maximum point as (B.3) does around $\vec{\kappa} = 0$. Each maximum thus contributes $\text{sgn}(\alpha_2)/2$ to the Chern number of the lower band.

Bibliography

[1] S. John, Phys. Rev. Lett. **58**, 2486 (1987)

[2] J. D. Joannopoulos, R. D. Meade, and J. N. Winn, *Photonic Crystals: Molding the Flow of Light.* Princeton University Press, 1995.

[3] W. A. Harrison, *Solid State Theory.* McGraw-Hill, 1970.

[4] E. Yablonovitch, Phys. Rev. Lett. **58**, 2059 (1987)

[5] P.S. Jessen and I.H. Deutsch, in *Advances in Atomic, Molecular, and Optical Physics*, B. Bederson and H. Walther ed. (Academic Press, Cambridge, 1996), vol. 37.

[6] D. Jaksch, C. Bruder, J. I. Cirac, C. W. Gardiner, and P. Zoller, Phys. Rev. Lett. **81**, 3108 (1998).

[7] I. H. Deutsch, R. J. C. Spreeuw, S. L. Rolston, and W. D. Phillips, Phys. Rev. A **52**, 1394 (1995).

[8] K. C. Huang, P. Bienstman, J. D. Joannopoulos, K. A. Nelson, and S. Fan, Phys. Rev. Lett. **90**, 196402 (2003).

[9] L.C. Andreani, Phys. Status Solidi B **188**, 29 (1995)

[10] M. Hübner, J. P. Prineas, C. Ell, P. Brick, E. S. Lee, G. Khitrova, H. M. Gibbs, and S. W. Koch, Phys. Rev. Lett. **83**, 2841 (1999).

[11] L. I. Deych and A. A. Lisyansky, Phys. Rev. B **62**, 4242 (2000).

[12] D. V. van Coevorden, R. Sprik, A. Tip, and A. Lagendijk, Phys. Rev. Lett. **77**, 2412 (1996).

[13] E. M. Purcell, Phys. Rev. **69**, 681 (1946).

[14] S. E. Harris, Phys. Today **50** (7), p.36 (1997).

[15] M. Fleischhauer and M. D. Lukin, Phys. Rev. Lett. **84**, 5094 (2000); Phys. Rev. A **65**, 022314 (2002).

[16] F. D. M. Haldane and S. Raghu, Phys. Rev. Lett. **100**, 013904 (2008).

[17] S. Raghu and F. D. M. Haldane, cond-mat/0602501.

[18] R. E. Prange and S. M. Girvin, ed. *The Quantum Hall Effect.* (Springer-Verlag, New York, 1987).

[19] M. Greiner, O. Mandel, T. Esslinger, T. W. Hänsch,

[20] J. J. Hopfield, Phys. Rev. **112**, 1555 (1958).

[21] C. W. Deutsche and C. A. Mead, Phys. Rev. **138**, A63 (1965).

[22] G. D. Mahan and G. Obermair, Phys. Rev. **183**, 834 (1969).

[23] J. Knoester and S. Mukamel, Phys. Rev. A **40**, 7065 (1989).

[24] E. Fermi, Rev. Mod. Phys. **4**, 87 (1932). and I. Bloch, Nature **415**, 39 (2002).

[25] D. F. Phillips, A. Fleischhauer, A. Mair, R. L. Walsworth, and M. D. Lukin, Phys. Rev. Lett. **86**, 783 (2001).

[26] C. Liu, Z. Dutton, C. H. Behroozi, and L. V. Hau, Nature **409**, 490 (2001).

[27] G. Juzeliūnas and H. J. Carmichael, Phys. Rev. A **65**, 021601(R) (2002).

[28] K. Sawada, Phys. Rev. **106**, 372 (1957); R. Brout, Phys. Rev. **108**, 515 (1957).

[29] A. Raczyński, J. Zaremba, and S. Zielśka-Kaniasty, Phys. Rev. A **69**, 043801 (2004).

[30] Z. Li, L. Xu, and K. Wang, Phys. Lett. A **346**, 269 (2005).

[31] E. A. Korsunsky and D. V. Kosachiov, Phys. Rev. A **60**, 4996 (1999).

[32] A. J. Merriam, S. J. Sharpe, M. Shverdin, D. Manuszak, G. Y. Yin, and S. E. Harris, Phys. Rev. Lett. **84**, 5308 (2000).

[33] P. Kolchin, Phys. Rev. A **75**, 033814 (2007).

[34] D. A. Braje, V. Balic, S. Goda, G. Y. Yin, and S. E. Harris, Phys. Rev. Lett. **93**, 183601 (2004).

[35] V. Balic, D. A. Braje, P. Kolchin, G. Y. Yin, and S. E. Harris, Phys. Rev. Lett. **94**, 183601 (2005).

[36] J. K. Thompson, J. Simon, H. Loh, and V. Vuletic, Science **313**, 74 (2006).

[37] Z. Wang, and S. F. Fan, *Opt. Lett.* **30**, 1989 (2005).

[38] I. L. Lyubchanskii *et. al.*, *J. Phys. D* **36**, R277 (2003).

[39] M. L. Povinelli *et. al.*, *Appl. Phys. Lett.* **84**, 3639 (2004).

[40] D. Thouless, M. Kohmoto, M. Nightingale, and M. den Nijs, Phys. Rev. Lett. **49**, 405 (1982).

[41] B. Simon, *Phys. Rev. Lett.* **51**, 2167 (1983).

[42] M. Kohmoto, Ann. Phys. (N. Y.) **160**, 355 (1985).

[43] Y. Hatsugai, *Phys. Rev. Lett.* **71**, 3697 (1993).

[44] M. Plihal and A. A. Maradudin, Phys. Rev. B **44** 8565 (1991).

[45] F. D. M. Haldane, Phys. Rev. Lett. **61**, 2015 (1988).

[46] D. M. Pozar, *Microwave Engineering* (John Wiley, New York, 1998).

[47] Comsol Multiphysics 3.3, COMSOL Inc.

[48] M. L. Povinelli *et. al.*, *Phys. Rev.* **B64**, 075313 (2001).

[49] E. P. Wohlfarth, in *Ferromagnetic Materials* , Vol. **2**, 293 (North-Holland, Amsterdam, 1986).

[50] S. G. Johnson and J. D. Joannopoulos, Opt. Express **8** 173 (2001).

[51] A. W. Joshi, *Elements of Group Theory for Physicists.* New Age, 2007.

[52] M. Onoda and N. Nagaosa, J. Phys. Soc. Japan **71**, 19 (2002).

[53] J. von Neumnann and E. Wigner, Phys. Z. **30**, 467 (1929).

[54] M. V. Berry, Proc. R. Soc. A**392**, 45 (1984).